Microbiota imprint gut–intrinsic neuronal programming and sympathetic activity

Paul A Muller[1,*], Zachary Kerner[1,‡], Marc Schneeberger[2,‡], and Daniel Mucida[1,*]

[1] Laboratory of Mucosal Immunology, The Rockefeller University, New York, NY 10065, USA

[2] Laboratory of Molecular Genetics, Howard Hughes Medical Institute, The Rockefeller University, New York, NY 10065, USA.

‡ These authors contributed equally to this work.

* Correspondence: pmuller@rockefeller.edu (P.A.M.), mucida@rockefeller.edu (D.M.)

Microbial density and diversity increases from proximal to distal regions of the intestine, affecting tissue physiology, metabolism, and function of the immune and nervous systems. Both intrinsic and extrinsic enteric–associated neurons (EAN) continuously monitor and modulate homeostatic intestinal functions, including nutrient absorption and motility. However, a systemic and circuit-based link between gut microbes and the nervous system has yet to be established. Through a combination of molecular, anatomic and functional approaches, we characterized the influence of the microbiota on EAN. We found that intrinsic EAN are functionally adapted to the specific intestinal region they occupy in a microbiota-dependent manner. Furthermore, we observed that gut–extrinsic sympathetic neurons are hyperactivated in the absence of microbes, while the production of butyrate is sufficient to suppress sympathetic activity. Finally, retrograde polysynaptic neuronal tracing from the intestinal wall revealed that brainstem GABAergic neurons are a potential central hub for modulation of gut–specific sympathetic neurons. These results reveal that commensal microbiota imprint gut–intrinsic neuronal gene programs and control extrinsic sympathetic activity through a metabolite–mediated gut-brain circuit.

Introduction

Enteric–associated neurons (EAN) comprise a numerous and heterogeneous population of neurons that monitor and respond to various environmental cues, including mechanical stretch and luminal metabolites, within the gastrointestinal (GI) tract[1,2]. The vast majority of luminal stimuli are derived from the diet and commensal microbes, which may be sensed directly by EAN fibers positioned along the intestinal epithelium. Luminal perturbations can also be transmitted to EAN indirectly, via signals derived from epithelial, glial, or immune cells inhabiting the same compartment[1,3]. Intrinsic EAN (iEAN), commonly referred to as the enteric nervous system (ENS), are neural crest–derived and organized in two distinct layers, the myenteric or Auerbach's plexus and submucosal or Meissner's plexus[2]. iEAN can operate autonomously and are primarily tasked with modulation of intestinal motility and secretory function[2]. Extrinsic EAN (eEAN) include sensory, parasympathetic, and sympathetic neurons the cell bodies of which reside outside of the intestine, but provide an additional layer of

control over gut function through extensive intestinal innervation. Further upstream, the central nervous system (CNS) can integrate synaptically–transmitted or circulating gut–derived signals, modulating intestinal physiology through stimulation of the hypothalamic–adrenal (HPA) axis and eEAN[2,4-8]. Recent studies have demonstrated that the gut microbiota influence the basal activity of intestine–associated cells, including the excitability of enteric associated neurons and the activation state of immune cells[2,3,7,9]. These interactions have also been implicated in several disease processes, ranging from irritable bowel syndrome to CNS diseases, such as Alzheimer's disease, Parkinson's disease and autism spectrum disorder[1,10-12]. These studies highlight the impact of the gut microbiota on EAN, however the cellular circuits and molecular components that mediate gut-EAN or gut–brain communication are still poorly understood.

We sought to determine how the microbiota impacts both iEAN and eEAN (Fig. 1a) to better characterize gut–specific neuronal circuits. Using neuronal–specific cell–sorting independent translating ribosomal affinity purification (TRAP)[13], we found that iEAN phenotypes are shaped by their physical location along the length of the intestine and by microbial perturbations. Furthermore, we demonstrate that sympathetic eEAN activity is tonically inhibited by the gut microbiota. Microbial depletion or germ–free conditions led to hyper-activation of sympathetic eEAN, which could be rescued by administering butyrate, a short–chain fatty acid produced in high concentrations by commensal microbiota. Intriguingly, our data also implicates eEAN sensory neurons as a source of microbial detection and brainstem GABAergic neurons as a potential central hub to control sympathetic neurons that selectively innervate the gut. This study outlines a potential gut-brain microbe detection circuit that operates via extrinsic sensory integration in the CNS to drive gut–directed sympathetic activity.

Compartmentalization of iEAN gene profiles

To profile iEAN, we opted for a TRAP approach[13]; cell type–specific mRNA profiling that bypasses the need for tissue fixation or single–cell suspension, avoiding possible confounding effects of neuronal dissociation on gene expression. We interbred pan–neuronal *Snap25*^{Cre} with *Rpl22*$^{lsl\text{-}HA}$ (RiboTag) mice[14], which express a hemagglutinin(HA)–tagged ribosomal subunit 22, allowing immunoprecipitation of actively–translated mRNA. Expression of HA–tagged ribosomes was confirmed in neurons in the myenteric plexus of *Snap25*^{RiboTag} mice (Fig. 1b). We confirmed successful immunoprecipitation (IP) of intact mRNA bound to HA-tagged ribosomes from myenteric neurons in the intestine muscularis, and RNA sequencing of bound transcripts revealed significant enrichment of neuronal-specific genes and pathways in *Cre*$^{+}$ compared to *Cre*$^{-}$ controls (Extended Data Fig. 1a-c). We found that the fidelity of the TRAP system also allows for the identification of novel enteric neuron markers such as CD9, which was confirmed to be highly expressed in EAN cell bodies and fibers in the myenteric plexus (Extended Data Fig. 1d). TRAP RNA-seq (TRAP-seq) analysis of iEAN (duodenum, ileum, colon) and eEAN (the nodose, NG and the celiac–superior mesenteric ganglia, CG-SMG) suggested that they possess distinct transcriptional profiles (Fig. 1c-e). Comparison between transcriptional profiles of myenteric neurons isolated from the duodenum, ileum, and colon revealed that iEANs segregated based on their anatomical location (Fig. 1f, g,

Extended Data Fig. 2a-d). Compartmentalized transcriptional profiles of myenteric neurons are consistent with the different functions for corresponding segments of the intestine. The proximal small intestine is highly absorptive, enriched with enteroendocrine cells (EECs) subtypes S, I and K, which produce secretin, cholecystokinin (CCK), ghrelin and glucose-dependent insulinotropic polypeptide (GIP), associated with lipid and nutrient absorption[15]. We found that duodenum iEAN, in comparison to ileum and colon, express significantly higher levels of transcripts encoding receptors involved in the response to proximal EEC–derived signals such as *Cckar*, *Gcgr*, and *Tacr3*, likely reflecting the duodenum's predominant role in nutrient absorption (Fig. 1g, Extended Data Fig. 2b, c). The terminal ileum and colon iEAN, in contrast, are enriched in neuropeptide transcripts involved in the control of secretomotor processes in the gut such as *Sst*, *Penk*, *Agrp*, *Grp,* and *Tac1* (Fig. 1g, Extended Data Fig. 2a-d). The site–specific imprinting of iEAN was also reflected in the enrichment of gene pathways and transcripts such as *Htr7*, encoding the serotonin 5-HT7 receptor, in colonic iEAN, possibly related to the high numbers of serotonin–producing enterochromaffin cells in the large intestine (Fig. 1g, Extended Data Fig. 2a-d). Immunofluorescence (IF) analysis confirmed this compartmentalization at the protein level: for instance, the neuropeptide somatostatin (SST), involved in the regulation of several GI hormones and smooth muscle contraction[16], is highly expressed in the ileum but scarcely expressed by duodenum EAN (Fig. 1h, i); while neuropeptide Y (NPY), involved in the regulation of food intake[16], was primarily expressed in the duodenum EAN (Fig. 1j, Extended Fig. 3a). Altogether, these data reveal that the distinct intestinal regions imprint a discrete gene expression profile on iEAN.

Microbiota–imprinting on iEAN

The density and diversity of the gut microbiota increases from the proximal to distal intestine, leading us to ask whether regionally distinct iEAN programs are partially influenced by the microbiota. To address the influence of microbial stimuli on EAN, we first performed AdipoClear[17] on whole–mount intestinal tissue followed by light-sheet microscopy to visualize the three-dimensional structure of EAN in the ileum and colon of germ–free (GF) or specific–pathogen free (SPF) mice. The overall organization of iEAN into the two distinct plexuses appeared unaltered between GF and SPF (Fig. 2a, Supplementary Video 1-4). We observed vast mucosal innervation in the small and large intestines of both GF and SPF mice reaching into individual villi with fibers adjacent to the epithelium (Fig. 2a). Analysis of the ileum indicated significant remodeling of nerve fibers reflecting the thin, blunted villi of GF animals, while colonic innervation did not show gross alterations between mice kept under GF and SPF conditions (Fig. 2a, Supplementary Video 1-4). To determine whether the microbiota impacts iEAN gene profiles, we re-derived *Snap25*^{RiboTag} mice under GF conditions (Extended Data Fig. 4a). Analysis of TRAP-seq from duodenum, ileum, and colon muscularis of GF *Snap25*^{RiboTag} mice suggested a large influence of microbiota on the compartmentalization of iEAN phenotypes. In SPF mice, principal component analysis clearly segregated proximal and distal intestinal regions. However, ileum, colon and duodenum samples from GF mice all clustered together with the duodenum samples of SPF mice, the region with the lowest microbial density (Fig. 2b). Analysis of the third principal component showed segregation of colon samples from the small intestine, which may reflect the presence of iEAN derived from sacral progenitors in the large intestine[18] (Extended Data Fig. 4b). In the

duodenum, only four genes were significantly upregulated in SPF compared to GF. In the ileum and colon, we detected 605 and 117 differentially–expressed genes upregulated, respectively, in SPF as compared to GF groups (Fig. 2c). Among these were genes encoding neuropeptides associated with a neuro-immune crosstalk and with EAN physiological function, such as *Nmu*[19] and *Sst* (Fig. 2c, d). SST protein expression changes were confirmed by IF of whole mount tissue from SPF and GF mice (Fig. 2e). Analysis of GF and SPF datasets using predicting associated transcription factors from annotated affinities (PASTAA) identified CREB amongst the most enriched transcription factors for the colon and ileum in SPF mice (Fig. 2f). Because the level of pCREB in neurons is often used as a direct measure of activation[20], we assessed phosphorylation of CREB (pCREB) at serine 133, key to inducing gene transcription, by IF. We found a significant reduction of pCREB in the ileum myenteric plexus of GF compared to SPF mice (Fig. 2g), suggesting that iEAN are hypoexcitable under gnotobiotic conditions, as previously demonstrated[21]. These results establish regional differences as well as the microbial influence on iEAN gene profiles, particularly on their neurochemical coding. The lack of significant changes in the microbial–sparse proximal intestine suggests that iEAN regional differences are largely determined by microbial stimulation.

Microbiota–derived butyrate inhibits gut sympathetic activation

The eEAN process information from multiple areas of the intestine simultaneously, and as such we posited that they might also be influenced by the microbiota. We next sought to better characterize the afferent and efferent circuits of eEAN. To identify and visualize eEAN cell bodies, we injected a fluorescent retrograde tracer, cholera toxin beta subunit (CTB), into the wall of the intestinal segments, and dissected extrinsic ganglia that project to the gut, specifically the nodose (NG), dorsal root (DRG), and celiac–superior mesenteric (CG-SMG) ganglion (Fig. 3a, Extended Data Fig. 5a, b). Dual fluorescent CTB tracers injected separately into the duodenum or ileum indicated that detection by sensory neurons in the NG and DRG is mediated by non-overlapping cell populations (Fig. 3b, Extended Data Fig 5c). We also observed distinct sympathetic neuronal populations projecting into different intestinal segments (Fig. 3b). These results highlight the compartmentalization of both sensory and effector eEAN. The eEAN locations defined here were utilized for TRAP profiling, aimed at characterizing possible microbial–imprinting on EAN.

Next, we performed TRAP-seq of the NG and CG-SMG isolated from GF and SPF *Snap25*^{RiboTag} mice. CG-SMG from GF animals showed significantly higher transcript levels of *Fos* and *Arc*, classical neuronal immediate–early genes, and indirect markers for neuronal activity (Fig. 3c). To assess sympathetic activation in the CG-SMG, we established a cFos–based neuronal–specific quantification using Fluorogold-injected mice subjected to stress (Extended Data Fig. 6a-c). CG-SMG isolated from GF mice displayed significantly more cFos^{+} neuronal nuclei than their SPF mice counterparts, reinforcing the TRAP-seq findings (Fig. 3d, e). Sympathetic hyperactivation in GF mice was further confirmed in mice obtained from a different gnotobiotic facility (Fig. 3e). A lack of CG-SMG neuronal activation was observed in SPF mice obtained from Taconic Biosciences and in-house SPF mice fed a diet matched to the one provided to mice in GF isolators (Fig. 3e).

The CG-SMG are part of the sympathetic arm of the autonomic nervous system, directly innervating the GI tract and are involved in several physiological functions including regulation of motility, secretion and blood flow[9]. We utilized multiple microbial manipulation strategies to address whether specific microbes, or their metabolites, could mediate tonic suppression of CG-SMG neurons. Fecal transfer from age, sex, strain, and diet–matched C57BL/6 SPF donors into C57BL/6 GF mice restored SPF CG-SMG neuronal tone to levels comparable to SPF conditions, indicating that microbiota suppress gut–extrinsic sympathetic neurons (Fig. 4a). However, the mere presence of bacteria is not sufficient to suppress CG-SMG neuronal activation, as evidenced by cFos levels observed in GF mice mono-colonized with segmented filamentous bacteria (SFB), which resembled GF mice (Fig. 4b). Colonization of GF with the defined altered–Schaedler–flora (ASF) consortium[22] mirrored the SPF phenotype (Fig. 4b). Sympathetic activation did not appear to be a result of a developmental alteration in GF mice, since microbiota depletion for 2 weeks using broad-spectrum antibiotics resulted in increased $cFos^{+}$ neurons in the CG-SMG when compared to Splenda– or water–treated control mice (Fig. 4c-e). Similar results were obtained using Fos^{GFP} reporter mice (Fig. 4d). Additionally, a single oral gavage of streptomycin to SPF C57BL/6 or BALB/c mice resulted in CG-SMG neuronal activation as early as 24 h post-gavage (Fig 4f). Five days post streptomycin treatment cFos levels in the CG-SMG returned to SPF baseline (Fig 4f). To confirm that activated sympathetic neurons projected to the intestine, we injected fluorescent CTB in the ileum of broad-spectrum antibiotic–treated or control Fos^{GFP} mice. The majority of CTB^{+} in the CG-SMG neurons were $cFos^{+}$ (Fig. 4e). The above results suggest that a complex microbiota, or specific bacterial species or metabolites, can inhibit gut–sympathetic neurons. Large shifts in the microbial community, even on a short time scale, appear to release this inhibition.

Several lines of evidence suggested that short–chain fatty acids (SCFA), especially butyrate, could be involved in the microbiota–induced regulation of sympathetic activation, including: increased microbiota–imprinting in iEAN from distal intestinal regions where SCFA accumulate[23]; gnotobiotic manipulations resulted in suppression of CG-SMG neurons when a complex mix of bacteria known to result in high levels of luminal butyrate[22,24]. We tested whether this metabolite could trigger sympathetic neuron inhibition by orally administering a stable form of butyrate, tributyrin, to GF mice or to SPF mice treated with streptomycin. In both cases, quantification of $cFos^{+}$ neurons in the CG-SMG revealed a significant reduction in activated neurons (Fig. 4g, h). These results identify SCFA as a likely physiological modulator of gut sympathetic neuronal activation.

Afferent circuitry of microbiota–dependent gut sympathetic neuron activation

We examined three possible pathways that could result in microbiota–dependent modulation of gut sympathetic neurons: i) direct sensing of the intestinal epithelium or mucosa by CG-SMG sympathetic neurons; ii) direct modulation of sympathetic neurons by CG-SMG–projecting iEAN (also known as viscerofugal neurons); iii) a CNS loop via afferent sensory neurons, brain and sympathetic preganglionic neurons (SPN) in the spinal cord[25].

i) To visualize the extent to which sympathetic innervation reaches the gut epithelium, we injected adeno-associated virus AAVrg-CAG-FLEX-tdTomato into the CG-SMG of *Snap25*^{Cre} mice, thereby restricting the expression of Tomato protein to neurons (Fig. 5a, Extended Data Fig 7a, b). As an independent and complementary strategy, AAVrg-hSyn1-Cre was injected into the CG-SMG of *Rosa*$^{lsl\text{-}tdTomato}$ mice (Extended Data Fig. 7c). In both approaches, we observed restriction of viruses to the ganglion and immediately surrounding tissue (Fig. 5a, Extended Data Fig 7c). Whole mount immunofluorescence or cleared–tissue imaging of the intestine showed innervation of the two neuronal plexuses, with sparse fibers extending to the mucosa, but no evidence of direct epithelial contact (Fig. 5b, c, Extended Data Fig. 7a-e, Supplementary Video 5-6), indicating that eEAN sympathetic neurons may not be positioned to directly detect signals from the epithelium. It remains plausible that signals such as butyrate diffuse through the gut tissue or act via the circulation to influence the CG-SMG activation. However, systemic (intraperitoneal) administration of tributyrin led instead to robust activation of the CG-SMG (Fig. 5d), as previously suggested[26]. These results suggest that direct detection by sympathetic neurons is not the primary mechanism of microbiota–mediated regulation of CG-SMG activation.

ii) We also addressed whether viscerofugal neurons directly regulate microbiota–dependent CG-SMG activation. We injected fluorescent CTB into the CG-SMG and identified a sparse population of CTB^{+} iEANs, likely viscerofugal, in the intestine muscularis[27] (Fig. 5e). To confirm that iEAN can make synaptic contacts with sympathetic neurons, we injected iEAN-tropic AAV6-CAG-FLEX-tdTomato[28] into the ileum of *Snap25*^{cre} mice (Fig. 5f). We detected tdTomato^{+} fibers within the CG-SMG, suggesting that viscerofugal neurons were capable of direct communication with sympathetic neurons (Fig. 5f). To assess a possible link between viscerofugal neurons and the activation of CG-SMG upon microbial depletion, we quantified activation markers in the myenteric plexus after antibiotic treatment. Oral gavage of streptomycin did not result in altered numbers of cFos^{+} neurons in the myenteric plexus when compared to PBS-control SPF mice (Fig. 5g). These experiments imply that in the absence of microbes, gut sympathetic neurons are activated by SPN (Extended Data Fig. 8), which are typically modulated by visceral sensory signals[29].

iii) Neuronal sensing at the intestinal epithelium and mucosa is primarily carried out by intrinsic primary afferent neurons and extrinsic sensory afferents[9]. We addressed whether sensing by afferent eEAN from the NG or DRG mediate tonic inhibition of gut sympathetic neurons by crossing SNS^{Cre}, a BAC-transgenic mouse expressing Cre under the *Scn10a* (*Nav1.8*) promoter[30], with inhibitory hM4Di (*Rosa*$^{lsl\text{-}hM4Di}$) designer receptors exclusively activated by designer drugs (DREADD) mice. With this strategy, administration of the synthetic G protein–coupled receptor (GPCR) ligand Compound 21 (C21) should result in the inhibition of afferent eEAN. We hypothesized that this inhibition would phenocopy the loss of microbial signals and thus lead to gut sympathetic neuron activation. We confirmed that SNS^{Cre} recombination targets most of DRG and NG neurons (data not shown) and also results in robust labeling of nerve fibers running along the intestinal epithelium and mucosa (Extended Data Fig. 9a, b). SNS^{hM4Di} mice displayed a significant activation of CG-SMG neurons upon administration of C21 (Fig. 5h). However, we observed that SNS^{Cre} targeted sympathetic neurons in the CG-SMG and sympathetic chain, raising the possibility that the effects observed in SNS^{Cre} mice could be due to direct effects in these ganglia (Extended Data

Fig. 9c). This is not a very probable mechanism, since sympathetic neurons in the CG-SMG do not seem to express either *Girk2*, thought to be a key component of hM4Di-driven inhibition[31], or *Chrm4*, the endogenous cholinergic muscarinic receptor 4 (data not shown). We also tested the outcome of hM4Di–mediated inhibition of sensory neurons using *Nav1.8*^{Cre} mice, a knock-in strain previously described to also target the majority (75%) of NG and DRG neurons[32]. In this strategy, we failed to detect robust activation of CG-SMG neurons following injection of C21 (Extended Data Fig. 9d). However, imaging of the intestine in *Nav1.8*^{tdTomato} reporter mice revealed sparse innervation of the epithelium and mucosa, suggesting that the population of sensory neurons targeted in these mice does not reach the layers directly exposed to microbial metabolites (Extended Data Fig 9a, b). We concluded that sympathetic activation in SNS^{hM4Di} mice is most likely the result of inhibition of a specific sensory neuron population not captured by the *Nav1.8*^{Cre} line. These results indicate that processes extended by sensory neurons through the gut mucosa may provide the initial afferent signal for modulation of efferent sympathetic activation.

Brainstem connection to gut sympathetic neurons

We hypothesized that sensory integration of intestine–derived signals in the CNS may result in tonic inhibition of gut sympathetic neurons. To define CNS regions upstream of sensory eEAN and gut sympathetic ganglia, we first injected fluorescent CTB into the CG-SMG and then performed whole–mount lightsheet imaging of the spinal cord. We observed CTB labeling within the interomediolateral cell column (IML), intercalated nucleus (IC), and central autonomic area (IPPe) (Fig. 6a, Supplementary Video 7), which constitute the SPN[25]. Next, we performed polysynaptic retrograde tracing by injecting pseudorabies virus PRV-614 [33], a PRV engineered to constitutively express red fluorescence protein (mRFP1) (PRV-RFP), into the ileum of SPF mice to locate neuronal populations that are synaptically connected to the intestine. Temporal analyses of viral transport provide a comprehensive view of neurons that compose neuronal networks. In these studies, the most proximal nodes in the circuit (with respect to intestine) are labeled at the earliest time points, whereas upstream nodes are labeled at later time points. Lightsheet imaging of the CG-SMG and intact spinal column (using calAdipoClear) showed RFP$^+$ cells within the CG-SMG and IML, IC, and IPPe after 3 days (Fig. 6b-d, Supplementary Video 8-9). We also analyzed the brain of PRV-RFP injected mice by AdipoClear tissue clearing (Fig. 6e) to identify the most downstream areas in the brain driving gut sympathetic tone. Using a modification of Clearmap analysis[34], we identified several brainstem regions first infected with PRV 4 days post infection, specifically the caudal raphe nuclei (involved in thermogenesis[35] and various gastrointestinal functions[36]), gigantocellular reticular nucleus (Gi), and lateral paragigantocellular nucleus (both thought to be involved in locomotion and gastrointestinal function[36,37]) (Fig. 6e, f, Extended Data Fig 10a, Supplementary Video 10). Analysis of the Allen Brain Atlas in-situ hybridization database pointed to *Vgat*$^+$ neurons, inhibitory neurons likely involved in the suppression of downstream neuronal networks synaptically connected to the intestine, including the CG-SMG[37], as the dominant population represented in our retrograde tracing. To confirm this possibility, we injected PRV-RFP into the ileum of *Slc32a1*$^{L10\text{-}GFP}$ (Vgat: inhibitory) mice. We observed colocalization of RFP$^+$/GFP$^+$ (retrograde labelled VGAT inhibitory) neurons in all three areas, although only in the gigantocellular nucleus the majority of retrograde labeled neurons were VGAT$^+$ (Fig. 6g-i).

Immunofluorescence of additional brainstem neuronal populations, such as vesicular glutamate transporter 2 (VGLUT2), confirmed that VGAT was the predominant population labeled (Extended Data Fig. 11). To address whether signals from different intestinal regions converge into distinct or similar neuronal populations in the brain, we injected PRV-RFP into the ileum and PRV-GFP into the colon (data not shown) or duodenum. We found that the majority of neurons in each of the three areas were labeled with both fluorescent proteins, suggesting a central hub that can control gut sympathetic neuronal activation (Fig. 6j, Extended Data Fig. 12a,b). Overall, these results identify a potential gut–brain circuit whereby commensal microbiota modulate gut sympathetic activation via brainstem regions.

Discussion

The influence of the gut microbiota encompasses a growing list including local nutrient absorption, activation of the gut–associated immune system, regulation of lipid metabolism, and systemic inflammatory disorders. In the nervous system, dysbiosis or depletion of commensal bacteria have been shown to impact iEAN excitability and neurochemical code[11,38], microglia maturation[39], CNS neurogenesis[12], and behavioral or cognitive disorders[10-12]. In addition to describing unique transcriptional program for iEAN compared to eEAN, our TRAP-seq approach revealed a microbial– and region–dependent iEAN gene profile along the intestine. Differences in iEAN programming along the intestine appear to be influenced by the specialized location they occupy, especially in the proximal regions. Therefore, iEAN adaptation to a highly absorptive proximal intestine environment may have a direct impact on the regulation of food intake, absorption and avoidance behavior[3,40].

The examination of actively–translated transcripts from iEAN isolated from GF and SPF mice in distinct anatomical locations pointed to the microbiota as a major driver of iEAN proximal versus distal programming. Duodenum iEAN samples were similar between GF and SPF mice, further supporting tissue imprinting by food-associated signals. On the other hand, distal iEAN displayed a suppressed phenotype in the absence of gut microbiota, including significant downregulation of transcripts encoding neuropeptides associated with immunomodulation, such as neuromedin U[19,41] and with control of intestine motility, such as SST[16]. The increased activation phenotype of distal iEAN in the presence of microbiota stimulation may be the result of direct sensing. Previous studies have demonstrated that neurons positioned at barrier surfaces can directly detect microbial–derived products such as N-formylated peptides and α-hemolysin[42], and our TRAP-seq of iEAN showed expression of transcripts encoding for the GPCR FFAR3 (GPR41), a butyrate receptor[23,43], although we failed to detect significant expression of transcripts encoding conventional pattern–recognition receptors. A local neuroepithelial circuit may constitute an additional sensing mechanism responsible for microbiota imprinting on EAN. Indeed, recent imaging analysis of PYY– and CCK–producing EECs suggested a direct synaptic–like interaction with EAN[44]. Intestinal epithelial cells, particularly EECs, are equipped to detect bacteria or their metabolites and to release neurotransmitters and neuropeptides in response to luminal challanges[15,44]. SCFA have been shown to activate serotonin–releasing enterochromaffin cells[45], and our EAN profiling indicates significant enrichment of transcripts

for the serotonin receptor HTR3a/b in duodenal and HTR7 in colonic iEAN. A combination of direct and indirect microbe–detection mechanisms, triggering gut–brain circuits uncovered in this study, may result in the activation of the autonomic nervous system or HPA axis impacting both CNS and gut physiology; therefore, dissecting such circuits represents one of the main challenges of the expanding gut–brain and microbiota fields. Our work provides novel perspective on how the distinct intestinal regions and their associated microbial environments impact the associated enteric nervous system.

The circuit and gene expression–based studies presented here contribute to the understanding of gut–brain communication by defining components of the circuit between the gut tissue, extrinsic sensory ganglia, the brain, and the sympathetic arm of the gut autonomic nervous system. Our results point to a role for microbial metabolites, particularly the SCFA butyrate, and sensory eEAN communication to the brain, in the regulation of gut–innervating sympathetic neurons. The effects ascribed to SCFA have been mostly associated with regulation of local gut immunity[23,43], but recent evidence also support a role for these metabolites in regulating local iEAN and intestinal motility[46,47] as well as CNS microglia and neuronal function[48]. Top-down control of sympathetic activity has been reported previously[9], the most evident demonstration of which occurs in cases of high spinal cord injury where a loss of brainstem inhibition leads to sympathetic amplification after normal sensory input and subsequent immune suppression[29,49]. Modulation of inhibitory neurons in the brainstem identified here could reduce spinal cord interneuron inhibition of preganglionic neurons[50,51]. Gut sympathetic activity can also impact blood flow, motility, and epithelial secretion[36,49], which in turn may influence microbial niches in the lumen. For instance, gut motility was recently described as a key driver of microbial colonization in zebrafish[52]. Our work suggests that EAN (direct or indirect) detection of microbes or their metabolites is a core sensory system whereby alterations in microbial composition can result in significant activation of gut–specific sympathetic neurons. Chemogenetic inhibition experiments presented here suggest that a particular population of gut epithelium–projecting sensory neurons play a role in mediating CNS–driven sympathetic suppression. An expanded description of iEAN and sensory eEAN populations involved in this circuit will likely require single-cell technology[53], circuit–based approaches and additional genetic tools. The precise characterization of the sensory neurons and associated brain regions that integrate signals from intestinal regions examined here, and the role of these regions in regulating gut sympathetic activity, may impact the understanding of the local regulation of intestinal motility, visceral pain, neuro–immune diseases and systemic disorders related to the gut–brain axis; knowledge essential in defining therapeutic strategies.

Methods

Mice. Wild-type mice used: C57Bl/6 (Jackson or Taconic) and Balb/C (Jackson). Transgenic mice used: *Fos*^{GFP} (B6.Cg-Tg(Fos/EGFP)1-3Brth, Jackson #014135), RiboTag (B6N.129-*Rpl22*$^{tm1.1Psam}$, Jackson #011029), *Snap25*^{cre}

(B6;129S-*Snap25*$^{tm2.1(cre)Hze}$, Jackson #023525), *Rosa26*$^{\text{lsl-hM4Di}}$ (B6N.129-*Gt(ROSA)26Sor*$^{tm1(CAG\text{-}CHRM4*,\text{-}mCitrine)Ute}$, Jackson #026219), *Rosa26*$^{\text{lsl-tdTomato}}$ (B6.Cg-*Gt(ROSA)26Sor*$^{tm14(CAG\text{-}tdTomato)Hze}$, Jackson #007914), *Vgat*^{cre} (*Slc32a1*$^{tm2(cre)Lowl}$, Jackson #016962), *Chat*^{cre} (B6;129S6-*Chat*$^{tm2(cre)Lowl}$, Jackson #006410). SNS^{cre} (Tg(*Scn10a*^{cre})1Rkun, Gift of R. Kuhner), *Nav1.8*^{cre} (*Scn10a*$^{\text{tm2(cre)Jnw}}$, gift of J Wood). Gnotobiotic mice used: Germ-Free (GF) C57Bl/6, *Snap25*^{RiboTag}, SFB-monocolonized, ASF colonized (Rockefeller University), GF C57Bl/6 (gift of J Faith, Mount Sinai School of Medicine). Mice were bred within our facility to obtain strains described and were 7-12 weeks of age for all experiments unless otherwise indicated. For comparisons to GF mice, mice were maintained on sterilized Autoclavable Mouse Breeder Diet (5021, LabDiet, USA), the same used in the gnotobiotic facility. Female mice were used for all sequencing experiments. Male and female mice were used for all other experiments. Animal care and experimentation were consistent with NIH guidelines and approved by the Institutional Animal Care and Use Committee (IACUC) at The Rockefeller University.

SFB colonization. Mice monocolonized with segmented filamentous bacteria (SFB) were kept in isolators and originally colonized by gavage with fecal extract from SFB monocolonized mice kept at NYU (Littman lab). SFB colonization was verified by real time PCR using SFB-specific 16S primers; GF feces served as a negative, Taconic Farms C57Bl/6 feces as a positive control.

Altered Schaedler Flora colonization. C57Bl/6 mice were maintained in germ-free conditions in ISOcage biocontainment isolator cages (Tecniplast, PA, USA) in the gnotobiotic facility at Rockefeller University. ASF colonization was achieved by inoculating germ-free mice with cecal contents of ASF donor mice stably colonized by vertical transmission (kindly provided by Amanda Ramer-Tait, University of Nebraska-Lincoln). Ceca were prepared by homogenization through a 100 um filter in sterile phosphate-buffered saline (PBS) at a ratio of one cecum per 1 ml of PBS. Mice received 200 ul of ASF inoculum via oral-gavage twice, one week apart. The presence of members of the ASF microbial community was confirmed by a real-time PCR-based assay previously described[54]. All mice were analyzed at least four weeks post colonization, with colonization further confirmed by 16s rRNA sequencing of both feces and ceca of analyzed mice. We could detect by qPCR and 16s RNA sequencing at least 6 species after colonization.

Antibiotic treatments. 0.25 g Vancomycin, 0.25 g metronidazole, 0.5 g ampicillin, and 0.5 g neomycin were dissolved in 500 mL of filtered water and supplemented with 5 g Splenda. To control for the sweet taste of the antibiotic solution, 5 g of Splenda was dissolved in filtered water. Water controls were given filtered water as their drinking water. All solutions were passed through a SteriCup 0.22 um filter. Streptomycin was prepared in sterile DPBS at a concentration of 200 mg/mL and then filtered with a 0.22 uM (EMD Millipore PES Express) syringe filter. A dose of 20 mg was given as an oral gavage of 100 uL of this stock solution.

Tributyrin treatment. Tributyrin (Sigma W222305-SAMPLE) was filter sterilized through a 0.22 uM (EMD

Millipore PES Express) syringe filter prior to oral gavage or i.p. injection. 200 uL of tributyrin were given by oral gavage[8]. Two oral gavages were given over a period of 24 h, with the second dose given 8 h before sacrifice.

Tracing injections. Mice were anesthetized with 4% Isoflourane with 1% oxygen followed by 2% isoflourane with 1% oxygen to maintain anesthesia. After shaving and sterilization of the abdomen, mice were placed on a sterile surgical pad on top of a heating pad and covered with a sterile surgical drape. Ophthalmic ointment was placed over the eyes to prevent dehydration and the incision site was sterilized. Upon loss of recoil paw compression, a midline incision was made through the abdominal wall exposing the peritoneal cavity. For injections into the CG-SMG or duodenum an additional incision was made laterally to allow for better access. The duodenum, ileum, colon, or celiac-superior mesenteric ganglion were located and exposed for injection. All injections were made with a pulled glass pipette using a Nanoject III. Following injection the abdominal wall was closed using absorbable sutures and the skin was closed using surgical staples. Antibiotic ointment was applied to the closed surgical site and mice were given 0.05 mg/kg buprenorphine every 12 h for 2 days.

Restraint stress. For restraint stress, each mouse was placed in a properly ventilated 50 mL conical plastic tube for 15 min. The mice could rotate, but could not turn head to tail.

Cholera toxin tracing. Mice were anesthetized and operated on as described above. 1.5 uL of 1% CTB 488, 555, or 647 in PBS with 0.1% FastGreen was injected with a pulled glass pipette using a Nanoject III into the ileum, duodenum, colon and celiac-superior mesenteric ganglion. Relevant tissues were then dissected after a minimum of 3 days post-injection.

Celiac ganglion tracing. Mice were anesthetized and operated on as described above. 1.5 uL of AAVrg-hSyn1-Cre with 0.1% FastGreen was injected into the CG-SMG of *Rosa26*$^{\text{lsl-tdTomato}}$ mice. 1.5 uL of AAV2-CAG-FLEX-tdTomato with 0.1% FastGreen was injected into the CG-SMG of *Snap25*^{cre} mice. Intestine samples were dissected after 2.5 weeks for AdipoClear, RIMS, or Focus Clear analysis.

Viscerofugal tracing. Mice were anesthetized and operated on as described above. 1.5 uL of AAV6-CAG-FLEX-tdTomato with 0.1% FastGreen was injected into the ileum wall of *Snap25*^{cre} mice. CG-SMG samples were then dissected after 2.5 weeks for whole mount immunofluorescence analysis.

Virus. The following viruses were used: AAV5-hSyn-DIO-hM4D(Gi)-mCherry (Addgene), AAV5-hSyn-DIO-mCherry (Addgene), AAVrg-CAG-tdTomato (Addgene), AAV6-CAG-FLEX-tdTomato (Addgene), AAVrg-hSyn1-Cre (Janelia), AAV2-CMV-Cre-EGFP (UNC Vector Core). Fast Green (Sigma) was added (0.1%) to virus injected into peripheral tissues.

Fluorogold Labeling. A stock solution of 4 mg/mL Fluorgold (Fluorochrome) was made in sterile 0.9% saline and then filter sterilized through a 0.22 um syringe filter. An i.p. injection of 300 uL of Fluorogold solution was given 3 days before tissue harvesting.

Retrograde PRV Tracing. Mice were anesthetized and operated on as described above. PRV Bartha 152 (GFP) or 614 (RFP) were a gift of L. Enquist. 3uL with 0.1% FastGreen was injected with a pulled glass pipette using a Nanoject III into the wall of the ileum, duodenum, and colon. Brains and spinal columns were harvested three and four days after injection.

Antibodies. The following primary antibodies were used, and unless otherwise indicated concentrations apply to all staining techniques: GFP Tag AF488/555/594/647 (1:400, Thermo Fisher Scientific A21311/A31851/A21312/A31852), TH (1:200, Aves Labs, TYH; 1:400, Millipore Sigma, AB152), BIII-Tubulin (1:400, Millipore Sigma, T2200; 1:200, Aves Labs, TUJ), NPY (1:200, Immunostar, 22940), SST (1:200, Millipore Sigma, MAB354), RFP (1:200, Sicgen, AB8181; 1:200 and 1:1000 AdipoClear brain, Rockland, 600-401-379), pCREB Ser133 (1:200, Cell Signaling Technologies, 9198S), ANNA-1 (1:200,000, Gift of Dr. Vanda A. Lennon), cFos (1:500, Cell Signaling Technologies, 2250S), HA (1:400, Cell Signaling Technologies, 3724S), 5-HT (1:200, Millipore Sigma, MAB352), and VGLUT2 (1:200, Millipore Sigma, AB2251-I). Fluorophore-conjugated secondary antibodies were either H&L or Fab (Thermo Fisher Scientific) at a consistent concentration of 1:400 in the following species and colors: goat anti-rabbit (AF488/568/647), goat anti-rat (AF488/647), goat anti-chicken (AF488/568/647), goat anti-human (AF568/647), donkey anti-guinea pig (AF488/647), donkey anti-rabbit (AF568/647), donkey anti-goat (AF568/647).

Intestine dissection. Mice were sacrificed and duodenum (4 cm moving proximal from the gastroduodenal junction), ileum (4 cm moving proximal from the ileocecal junction), or colon (4 cm moving proximal from the rectum) was removed. For AdipoClear fecal contents were flushed from the lumen and left intact. Tissue used for RIMS or FocusClear were cut open longitudinally and fecal contents were washed out. For dissection of the muscularis, following the above procedures, the intestinal tissue was placed on a chilled aluminum block with the serosa facing up[6]. Curved forceps were then used to carefully remove the *muscularis*.

Nodose ganglion dissection. Mice were sacrificed and the ventral neck surface was cut open. Associated muscle was removed by blunt dissection to expose the trachea and the nodose ganglion was then located by following the vagus nerve along the carotid artery to the base of the skull. Fine scissors were used to cut the vagus nerve below the nodose ganglion and superior to the jugular ganglion.

Celiac-superior mesenteric ganglion dissection. Mice were sacrificed and a midline incision was made and the viscera were reflected out of the peritoneal cavity. The intersection of the descending aorta and left renal artery was

identified, from which the superior mesenteric artery was located. The CG-SMG is wrapped around the superior mesenteric artery and associated lymphatic vessels. Fine forceps and scissors were used to remove the CG-SMG.

Dorsal root ganglion dissection. The spinal column was isolated, cleaned of muscle, and bisected sagittally. The spinal cord was removed leaving the dorsal root ganglion (DRG) held in place by the meninges. The thoracic 13 DRG was identified by its position just caudal to thoracic vertebra. The meninges were cleared and individual DRGs were removed with fine forceps and scissors.

Spinal cord dissection. For 3DISCO analysis the spinal cord was isolated by hydraulic extrusion as previously described[55]. For whole spinal column calAdipoClear imaging, the entire spinal column was removed with associated tissue. Costae and muscle were carefully trimmed to reduce the size of the sample to fit into a 5 mL Eppendorf tube while avoiding disrupt ventral tissue attached to the spinal cord.

RiboTag. Heterozygous or homozygous *Snap25*^{RPL22HA} were used for TRAP-seq analysis as no differences were found between either genotype. For intestine immunoprecipitation (IP) mice were sacrificed and tissue remove and divided as above. Samples were washed of fecal contents in PBS with cycloheximide (0.2 mg/mL) (PBS/CHX). Mesenteric fat was removed and the *muscularis* was separated from the mucosa as described above and samples were washed 5 times in PBS/CHX. For nodose and CG-SMG IP, tissues were isolated as described above. The RiboTag IP protocol was then followed (http://depts.washington.edu/mcklab/RiboTagIPprotocol2014.pdf) with the following modifications. All samples were homogenized by hand with a dounce homogenizer in 2.5 mL supplemented homogenization buffer (changes per 2.5 mL: 50 uL Protease Inhibitor, 75 uL heparin (100 mg/mL stock), 25 uL SUPERase• In RNase Inhibitor). Samples were then centrifuged for 10 minutes at 10,000 G, after which 800 uL of supernatant was removed and 5uL of anti-HA antibody (Abcam, ab9110) was added. Samples were kept rotating at 4°C with antibody for 1 hour. 200 uL of Thermo Protein magnetic A/G beads were washed with homogenization buffer, added to the sample, and kept rotating for 30 minutes at 4°C. The beads were washed four times with high-salt buffer and samples were eluted with 100 uL of PicoPure lysis buffer. RNA was extracted using the Arcturus PicoPure RNA isolation kit (Applied Biosystems) according to the manufacturer's instructions.

RNA-sequencing. RNA libraries were prepared using SMARTer Ultra Low Input RNA (ClonTech Labs) and sequenced using 75 base-pair single end reads on a NextSeq 500 instrument (Illumina). Reads were aligned using Kallisto[56] to Mouse Ensembl v91. Transcript abundance files were then used in the DESeq2 R package, which was used for all downstream differential expression analysis and generation of volcano plots. For intestine samples Cre+ samples were compared with Cre- samples to generate a list of immunoprecipitated (IP) enriched genes (log2FC > 1 and padj < 0.05). This IP enriched list was then used to perform downstream analysis. Differentially expressed genes between samples were defined as those contained within the total IP enriched list from tissues being compared and with a cutoff of log2FC > 1. PCA plots were generated from log transformed DEseq2 data, as

indicated in figure legends, with the FactoMineR R package. GSEA pre-ranked analysis was performed with desktop software and the C5 gene ontology database using 1000 permutations. Gene ontology enrichment analysis was performed with differentially expressed genes (log2FC > 1, padj < 0.05) using the TopGO R package and a Fisher test with an elimination algorithm was used to calculate significance.

PASTAA analysis. Differentially expressed Ensembl gene ID lists (log2FC > 1, padj < 0.05) from ileum and colon samples (GF vs SPF) were used in the Predicting Associated Transcription factors from Annotated Affinities (PASTAA) web tool (http://trap.molgen.mpg.de/PASTAA.htm). Significant (p-value < 0.05) association scores for transcription factors were plotted.

Brain immunofluorescence. Mice were sacrificed and transcardially perfused with cold PBS with heparin followed by cold 4% PFA. The intact brain was separated carefully from the skull and placed in 4% PFA, and then rotated for 48 h at 4°C. Whole brains were washed with PBS and sectioned at 50 µm on a Leica vibrotome for immunofluorescence. Samples were then permeabilized in 0.5% Triton/0.05 Tween-20 in PBS (PTx) followed by blocking in 5% goat serum in PTx each for 2 h at room temperature. Primary antibody was added to the blocking buffer and samples were incubated with constant rotation at 4°C overnight. Four 15-minute washes were done in PTx at RT after which samples were moved to blocking buffer with secondary antibody. Slices were incubated in secondary antibody for 2 hours at room temperature followed by four 15 minute washes in PTx at room temperature. Samples were then placed on glass slides, covered in Fluormount G, and coverslipped.

Confocal imaging. Whole mount intestine, NG, DRG, and CG-SMG samples were imaged on an inverted LSM 880 NLO laser scanning confocal and multiphoton microscope (Zeiss)**.**

RIMS clearing. Briefly, following secondary staining CG-SMG, nodose and DRG were submerged in Refractive Index Matching Solution (RIMS) for 30-120 min then mounted in RIMS solution on a glass slide and sealed with a coverslip for confocal imaging[29].

FocusClear. Whole intestine and celiac ganglion samples were first fixed in 4% PFA overnight at 4°C. Samples were then washed three times in DPBS at RT. Samples were placed into 250 uL of FocusClear solution for 15-20 minutes. They are then transferred to MountClear solution on a glass slide and a 1 ½ coverslip was used to seal the sample in place.

3DISCO. 3DISCO clearing of whole spinal cord was done as previously described [57].

AdipoClear. Adipoclear whole tissue clearing was adapted from Adipoclear protocol[11]. Mice were sacrificed and intestinal sections were removed followed by overnight fixation in 4% PFA. Tissues were washed in PBS then

dehydrated in 20/40/60/80/100% Methanol in B1N followed by dichloromethane. Tissues were then rehydrated in 100/80/60/40/20% methanol in B1N. Subsequently, samples were washed in PTxwH and then incubated in primary antibody dilutions in PTxwH for 7 Days. Samples were washed in PTxwH then incubated in secondary antibody at 1:400 in PTxwH for 7 days. Samples were again washed in PTxwH followed by PBS then dehydrated in 20/40/60/80/100% methanol followed by dichloromethane and finally cleared in dibenzyl ether.

calAdipoClear. CalAdipoclear whole tissue clearing was adapted from Adipoclear protocol[17]. Briefly, mice were sacrificed and perfused with PBS followed by 4% PFA. Whole spinal columns were removed and put into 4% PFA overnight. Tissues were washed in PBS then dehydrated in 20/40/60/80/100% methanol in B1N followed by dichloromethane. Tissues were then rehydrated in 100/80/60/40/20% methanol in B1N. Subsequently, samples were decalcified in Morse Solution (1 part 45% formic acid/1 part 0.68 mM sodium citrate dihydrate) overnight followed by PTxwH washes. Samples were then incubated in primary antibody dilutions in PTxwH for 7 Days. Samples were washed in PTxwH then incubated in secondary antibody at 1:400 in PTxwH for 7 days. Samples were again washed in PTxwH followed by PBS then dehydrated in 20/40/60/80/100% methanol followed by dichloromethane and finally cleared in dibenzyl ether.

Light-sheet microscopy and 3D reconstruction. Whole-tissue cleared samples were imaged submerged in DBE on a LaVision Biotech Ultramicroscope II with 488 nm, 561nm or 647 nm light-sheet illumination using a 1.3x or 4x objective with 2.5um Z-slices. Images were adjusted post hoc using Imaris x64 software (version 9.1 Bitplane) and 3D reconstructions were recorded as mp4 video files. Optical slices were taken using the orthoslicer or oblique slicer tool.

ClearMap analysis. All analyses for whole-brain studies were performed adapting ClearMap pipeline (latest version available from www.idisco.info, see also[34].

cFos counting. Mice were sacrificed by cervical dislocation and CG-SMG were harvested and fixed overnight in 4% PFA. CG-SMG were then washed four times in DPBS at RT and permeabilized in PTxwH for 4 h at RT. Primary antibody cFos (1:500, Cell Signaling Technologies, 2250S) was added to the samples in PTxwH and incubated at 4°C for 48 h. Samples were washed four times in PTxwH at RT and then stained with goat-anti rabbit AF555/568/647 at 4°C for 48 h. Samples were washed four times in PTxwH at RT, covered in Fluormount G, and coverslipped for confocal imaging. We attempted to capture all sympathetic neurons within the CG-SMG with multiple z-stack images. We first established criteria for identifying neuronal cFos+ nuclei by staining CG-SMG from restraint-stressed mice. FluoroGold was used to identify sympathetic neurons and cFos+ nuclei were defined as morphologically circular with a diameter of 8-14um. These criteria were sufficient to distinguish between small intensely fluorescent cells and possibly macrophages that also have cFos expression. All images were analyzed in Image-J. Total cfos+ nuclei were counted using the Cell Counter plugin for Image-J. Each data point represents

the number of cfos+ cells per CG-SMG.

DREADD agonist. Water soluble Compound 21 (HelloBio) was dissolved in sterile 0.9% saline. Mice were given an intraperitoneal injection at a dose of 10 mg/kg.

Statistical analysis. Significance levels indicated are as follows: *P < 0.05, **P < 0.01, ***P < 0.001. All data are presented as mean ± s.d.. All statistical tests used were two-tailed. The experiments were not randomized and no statistical methods were used to predetermine sample size. Multivariate data was analyzed by one-way ANOVA and Tukey's multiple comparisons post hoc test. Comparisons between two conditions were analyzed by unpaired Student's t-test. We used GraphPad PRISM version 7.0d and R 3.4.3 for generation of graphs and statistics.

References

1 Mayer, E. A. Gut feelings: the emerging biology of gut-brain communication. *Nat Rev Neurosci* **12**, 453-466, doi:10.1038/nrn3071 (2011).

2 Furness, J. B., Rivera, L. R., Cho, H. J., Bravo, D. M. & Callaghan, B. The gut as a sensory organ. *Nature reviews. Gastroenterology & hepatology* **10**, 729-740, doi:10.1038/nrgastro.2013.180 (2013).

3 Veiga-Fernandes, H. & Mucida, D. Neuro-Immune Interactions at Barrier Surfaces. *Cell* **165**, 801-811, doi:10.1016/j.cell.2016.04.041 (2016).

4 Williams, E. K. *et al.* Sensory Neurons that Detect Stretch and Nutrients in the Digestive System. *Cell*, doi:10.1016/j.cell.2016.05.011 (2016).

5 Fung, T. C., Olson, C. A. & Hsiao, E. Y. Interactions between the microbiota, immune and nervous systems in health and disease. *Nature neuroscience* **20**, 145-155, doi:10.1038/nn.4476 (2017).

6 Gabanyi, I. *et al.* Neuro-immune Interactions Drive Tissue Programming in Intestinal Macrophages. *Cell* **164**, 378-391, doi:10.1016/j.cell.2015.12.023 (2016).

7 Rankin, L. C. & Artis, D. Beyond Host Defense: Emerging Functions of the Immune System in Regulating Complex Tissue Physiology. *Cell* **173**, 554-567, doi:10.1016/j.cell.2018.03.013 (2018).

8 Moriyama, S. *et al.* beta2-adrenergic receptor-mediated negative regulation of group 2 innate lymphoid cell responses. *Science* **359**, 1056-1061, doi:10.1126/science.aan4829 (2018).

9 Pavlov, V. A., Chavan, S. S. & Tracey, K. J. Molecular and Functional Neuroscience in Immunity. *Annual review of immunology* **36**, 783-812, doi:10.1146/annurev-immunol-042617-053158 (2018).

10 Kim, S. *et al.* Maternal gut bacteria promote neurodevelopmental abnormalities in mouse offspring. *Nature* **549**, 528-532, doi:10.1038/nature23910 (2017).

11 Yano, J. M. *et al.* Indigenous bacteria from the gut microbiota regulate host serotonin biosynthesis. *Cell* **161**, 264-276, doi:10.1016/j.cell.2015.02.047 (2015).

12 Hsiao, E. Y. *et al.* Microbiota modulate behavioral and physiological abnormalities associated with neurodevelopmental disorders. *Cell* **155**, 1451-1463, doi:10.1016/j.cell.2013.11.024 (2013).

13 Heiman, M., Kulicke, R., Fenster, R. J., Greengard, P. & Heintz, N. Cell type-specific mRNA purification by translating ribosome affinity purification (TRAP). *Nature protocols* **9**, 1282-1291, doi:10.1038/nprot.2014.085 (2014).

14 Sanz, E. *et al.* Cell-type-specific isolation of ribosome-associated mRNA from complex tissues. *Proceedings of the National Academy of Sciences of the United States of America* **106**, 13939-13944, doi:10.1073/pnas.0907143106 (2009).

15 Gribble, F. M. & Reimann, F. Enteroendocrine Cells: Chemosensors in the Intestinal Epithelium. *Annual review of physiology* **78**, 277-299, doi:10.1146/annurev-physiol-021115-105439 (2016).

16 Grider, J. R. Neurotransmitters mediating the intestinal peristaltic reflex in the mouse. *The Journal of pharmacology and experimental therapeutics* **307**, 460-467, doi:10.1124/jpet.103.053512 (2003).
17 Chi, J. *et al.* Three-Dimensional Adipose Tissue Imaging Reveals Regional Variation in Beige Fat Biogenesis and PRDM16-Dependent Sympathetic Neurite Density. *Cell metabolism* **27**, 226-236 e223, doi:10.1016/j.cmet.2017.12.011 (2018).
18 Obermayr, F., Hotta, R., Enomoto, H. & Young, H. M. Development and developmental disorders of the enteric nervous system. *Nature reviews. Gastroenterology & hepatology* **10**, 43-57, doi:10.1038/nrgastro.2012.234 (2013).
19 Cardoso, V. *et al.* Neuronal regulation of type 2 innate lymphoid cells via neuromedin U. *Nature* **549**, 277-281, doi:10.1038/nature23469 (2017).
20 Cohen, S. M. *et al.* Excitation-Transcription Coupling in Parvalbumin-Positive Interneurons Employs a Novel CaM Kinase-Dependent Pathway Distinct from Excitatory Neurons. *Neuron* **90**, 292-307, doi:10.1016/j.neuron.2016.03.001 (2016).
21 McVey Neufeld, K. A., Mao, Y. K., Bienenstock, J., Foster, J. A. & Kunze, W. A. The microbiome is essential for normal gut intrinsic primary afferent neuron excitability in the mouse. *Neurogastroenterology and motility : the official journal of the European Gastrointestinal Motility Society* **25**, 183-e188, doi:10.1111/nmo.12049 (2013).
22 Dewhirst, F. E. *et al.* Phylogeny of the defined murine microbiota: altered Schaedler flora. *Applied and environmental microbiology* **65**, 3287-3292 (1999).
23 Smith, P. M. *et al.* The microbial metabolites, short-chain fatty acids, regulate colonic Treg cell homeostasis. *Science* **341**, 569-573, doi:10.1126/science.1241165 (2013).
24 Biggs, M. B. *et al.* Systems-level metabolism of the altered Schaedler flora, a complete gut microbiota. *ISME J* **11**, 426-438, doi:10.1038/ismej.2016.130 (2017).
25 Deuchars, S. A. & Lall, V. K. Sympathetic preganglionic neurons: properties and inputs. *Compr Physiol* **5**, 829-869, doi:10.1002/cphy.c140020 (2015).
26 Kimura, I. *et al.* Short-chain fatty acids and ketones directly regulate sympathetic nervous system via G protein-coupled receptor 41 (GPR41). *Proceedings of the National Academy of Sciences of the United States of America* **108**, 8030-8035, doi:10.1073/pnas.1016088108 (2011).
27 Hibberd, T. J., Zagorodnyuk, V. P., Spencer, N. J. & Brookes, S. J. Identification and mechanosensitivity of viscerofugal neurons. *Neuroscience* **225**, 118-129, doi:10.1016/j.neuroscience.2012.08.040 (2012).
28 Benskey, M. J. *et al.* Targeted gene delivery to the enteric nervous system using AAV: a comparison across serotypes and capsid mutants. *Molecular therapy : the journal of the American Society of Gene Therapy* **23**, 488-500, doi:10.1038/mt.2015.7 (2015).
29 Ueno, M., Ueno-Nakamura, Y., Niehaus, J., Popovich, P. G. & Yoshida, Y. Silencing spinal interneurons inhibits immune suppressive autonomic reflexes caused by spinal cord injury. *Nature neuroscience* **19**, 784-787, doi:10.1038/nn.4289 (2016).
30 Chiu, I. M. *et al.* Transcriptional profiling at whole population and single cell levels reveals somatosensory neuron molecular diversity. *Elife* **3**, doi:10.7554/eLife.04660 (2014).
31 Roth, B. L. DREADDs for Neuroscientists. *Neuron* **89**, 683-694, doi:10.1016/j.neuron.2016.01.040 (2016).
32 Shields, S. D. *et al.* Nav1.8 expression is not restricted to nociceptors in mouse peripheral nervous system. *Pain* **153**, 2017-2030, doi:10.1016/j.pain.2012.04.022 (2012).
33 Banfield, B. W., Kaufman, J. D., Randall, J. A. & Pickard, G. E. Development of pseudorabies virus strains expressing red fluorescent proteins: new tools for multisynaptic labeling applications. *J Virol* **77**, 10106-10112 (2003).
34 Renier, N. *et al.* Mapping of Brain Activity by Automated Volume Analysis of Immediate Early Genes. *Cell*, doi:10.1016/j.cell.2016.05.007 (2016).
35 Morrison, S. F. & Nakamura, K. Central neural pathways for thermoregulation. *Front Biosci (Landmark Ed)* **16**, 74-104 (2011).
36 Browning, K. N. & Travagli, R. A. Central nervous system control of gastrointestinal motility and secretion and modulation of gastrointestinal functions. *Compr Physiol* **4**, 1339-1368, doi:10.1002/cphy.c130055 (2014).
37 Capelli, P., Pivetta, C., Soledad Esposito, M. & Arber, S. Locomotor speed control circuits in the caudal brainstem. *Nature* **551**, 373-377, doi:10.1038/nature24064 (2017).

38 McVey Neufeld, K. A., Perez-Burgos, A., Mao, Y. K., Bienenstock, J. & Kunze, W. A. The gut microbiome restores intrinsic and extrinsic nerve function in germ-free mice accompanied by changes in calbindin. *Neurogastroenterology and motility : the official journal of the European Gastrointestinal Motility Society* **27**, 627-636, doi:10.1111/nmo.12534 (2015).
39 Matcovitch-Natan, O. *et al.* Microglia development follows a stepwise program to regulate brain homeostasis. *Science* **353**, aad8670, doi:10.1126/science.aad8670 (2016).
40 Palm, N. W., Rosenstein, R. K. & Medzhitov, R. Allergic host defences. *Nature* **484**, 465-472, doi:10.1038/nature11047 (2012).
41 Klose, C. S. N. *et al.* The neuropeptide neuromedin U stimulates innate lymphoid cells and type 2 inflammation. *Nature* **549**, 282-286, doi:10.1038/nature23676 (2017).
42 Chiu, I. M. *et al.* Bacteria activate sensory neurons that modulate pain and inflammation. *Nature* **501**, 52-57, doi:10.1038/nature12479 (2013).
43 Arpaia, N. *et al.* Metabolites produced by commensal bacteria promote peripheral regulatory T-cell generation. *Nature* **504**, 451-455, doi:10.1038/nature12726 (2013).
44 Bohorquez, D. V. *et al.* Neuroepithelial circuit formed by innervation of sensory enteroendocrine cells. *The Journal of clinical investigation* **125**, 782-786, doi:10.1172/JCI78361 (2015).
45 Bellono, N. W. *et al.* Enterochromaffin Cells Are Gut Chemosensors that Couple to Sensory Neural Pathways. *Cell* **170**, 185-198 e116, doi:10.1016/j.cell.2017.05.034 (2017).
46 Soret, R. *et al.* Short-chain fatty acids regulate the enteric neurons and control gastrointestinal motility in rats. *Gastroenterology* **138**, 1772-1782, doi:10.1053/j.gastro.2010.01.053 (2010).
47 Wichmann, A. *et al.* Microbial modulation of energy availability in the colon regulates intestinal transit. *Cell host & microbe* **14**, 582-590, doi:10.1016/j.chom.2013.09.012 (2013).
48 Erny, D. *et al.* Host microbiota constantly control maturation and function of microglia in the CNS. *Nature neuroscience* **18**, 965-977, doi:10.1038/nn.4030 (2015).
49 Straub, R. H., Wiest, R., Strauch, U. G., Harle, P. & Scholmerich, J. The role of the sympathetic nervous system in intestinal inflammation. *Gut* **55**, 1640-1649, doi:10.1136/gut.2006.091322 (2006).
50 Schramm, L. P. Spinal sympathetic interneurons: their identification and roles after spinal cord injury. *Prog Brain Res* **152**, 27-37, doi:10.1016/S0079-6123(05)52002-8 (2006).
51 Spanswick, D., Pickering, A. E., Gibson, I. C. & Logan, S. D. Inhibition of sympathetic preganglionic neurons by spinal glycinergic interneurons. *Neuroscience* **62**, 205-216 (1994).
52 Logan, S. L. *et al.* The Vibrio cholerae type VI secretion system can modulate host intestinal mechanics to displace gut bacterial symbionts. *Proceedings of the National Academy of Sciences of the United States of America* **115**, E3779-E3787, doi:10.1073/pnas.1720133115 (2018).
53 Hockley, J. R. F. *et al.* Single-cell RNAseq reveals seven classes of colonic sensory neuron. *Gut*, doi:10.1136/gutjnl-2017-315631 (2018).
54 Gomes-Neto, J. C. *et al.* A real-time PCR assay for accurate quantification of the individual members of the Altered Schaedler Flora microbiota in gnotobiotic mice. *J Microbiol Methods* **135**, 52-62, doi:10.1016/j.mimet.2017.02.003 (2017).
55 Kennedy, H. S., Jones, C., 3rd & Caplazi, P. Comparison of standard laminectomy with an optimized ejection method for the removal of spinal cords from rats and mice. *J Histotechnol* **36**, 86-91, doi:10.1179/014788813X13756994210382 (2013).
56 Bray, N. L., Pimentel, H., Melsted, P. & Pachter, L. Near-optimal probabilistic RNA-seq quantification. *Nature biotechnology* **34**, 525-527, doi:10.1038/nbt.3519 (2016).
57 Erturk, A. *et al.* Three-dimensional imaging of solvent-cleared organs using 3DISCO. *Nature protocols* **7**, 1983-1995, doi:10.1038/nprot.2012.119 (2012).

Acknowledgements

We thank all Mucida Lab members past and present for assistance in experiments, fruitful discussions and critical reading of the manuscript, Aneta Rogoz for the maintenance of gnotobiotic mice, Sara Gonzalez for maintenance of

SPF mice, Tomiko Rendon and Beatriz Lopez for genotyping, Carla Nowosad for setting up the ASF mice, the Rockefeller University Bio-imaging Research Center for assistance with the light sheet microscopy and image analysis, the Rockefeller University Genomics Center for RNA sequencing and the Rockefeller University employees for continuous assistance. We thank Jeffrey Friedman (Rockefeller University) for the generous use of lab equipment. We thank Putianqi Wang (Rockefeller University) for important input on experimental design. We thank Ainsley Lockhart and Veronica Jové (Rockefeller University) for critical reading of the manuscript. We also thank Michel Nussenzweig, Gabriel Victora (Rockefeller University) and Juan Lafaille (NYU) and their respective lab members for fruitful discussions and suggestions. We are also indebted to Dan Littman and Mo Xu (NYU) for generously providing feces from SFB monocolonized mice; and Amanda Ramer-Tait (UNL) for ASF ceca. This work was supported NIH Virus Center grant no. P40 OD010996, NIH F31 Kirchstein Fellowship (P.A.M.), NCATS NIH UL1TR001866 (P.A.M., D.M.), Philip M. Levine Fellowship (P.A.M.), Kavli Graduate Fellow (P.A.M.), Kavli Postdoctoral Fellow (M.S.), the Leona M. and Harry B. Helmsley Charitable Trust (D.M.), the Burroughs Wellcome Fund PATH Award (D.M.), Transformative R01DK116646 (D.M.).

Author Contributions

P.A.M. initiated, designed, performed and analyzed the research, and wrote the manuscript. Z.K. performed experiments, analysis and helped with manuscript preparation. M.S. performed brain AdipoClear and ClearMap analysis, provided guidance on brain experiments and helped with manuscript preparation. D.M. initiated, designed and supervised the research, and wrote the manuscript.

Competing interests

The authors declare no competing financial interests.

Materials & Correspondence

Paul Muller (pmuller@rockefeller.edu) or Daniel Mucida (mucida@rockefeller.edu)

Supplementary Video Legends

Supplementary Video 1. AdipoClear whole mount SPF ileum stained with anti-TUJ1.

Supplementary Video 2. AdipoClear whole mount GF ileum stained with anti-TUJ1.

Supplementary Video 3. AdipoClear whole mount SPF colon stained with anti-TUJ1.

Supplementary Video 4. AdipoClear whole mount GF colon stained with anti-TUJ1.

Supplementary Video 5. AdipoClear whole mount of colon stained with anti-RFP showing tdTomato+ fibers from the CG-SMG 2 weeks post AAVrg-CAG-FLEX-tdTomato injection.

Supplementary Video 6. AdipoClear whole mount of cecum stained with anti-RFP showing tdTomato+ fibers from the CG-SMG 2 weeks post AAVrg-CAG-FLEX-tdTomato injection.

Supplementary Video 7. 3DISCO whole mount of spinal cord with neurons retrograde traced from the CG-SMG with CTB555.

Supplementary Video 8. calAdipoClear whole mount of spinal cord stained with anti-RFP (red) and anti-TH (green), showing the CG-SMG 4 days post PRV infection in the ileum.

Supplementary Video 9. calAdipoClear whole mount of spinal cord stained with anti-RFP (red) and anti-TH (white) 4 days post PRV infection in the ileum.

Supplementary Video 10. AdipoClear whole mount of brain stained with anti-RFP (red) 3 and 4 days post PRV infection in the ileum, showing the brainstem.

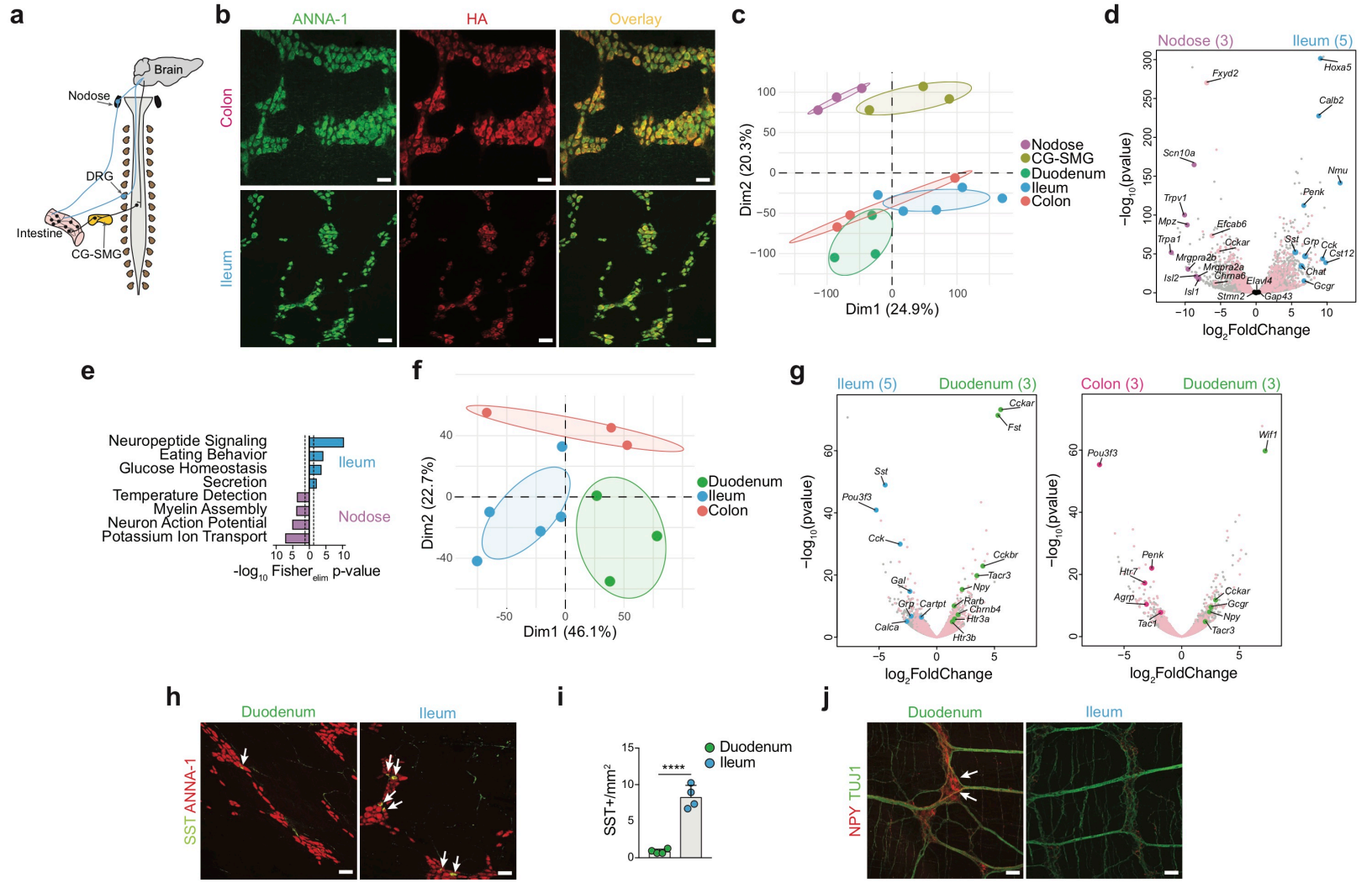

Figure 1 | TRAP-seq profiling of iEAN reveals anatomical imprinting. a, Anatomical diagram of intrinsic and extrinsic EAN. Blue lines highlight afferent fibers and black lines highlight efferent fibers. DRG = dorsal root ganglion,CG-SMG = celiac-superior mesenteric ganglion. **b**, Immunofluorescence staining of myenteric plexus neurons from the ileum and colon of *Snap25*^{RiboTag} SPF mice using anti-hemagglutinin (HA) and anti-neuronal nuclear (ANNA-1) antibodies. Scale bars = 50 µm. Images representative of at least n=3. **c**, Principal Component Analysis of translatomes from nodose ganglion, celiac-superior mesenteric ganglion, duodenum, ileum, and colon EAN of *Snap25*^{RiboTag} SPF mice. **d**, Volcano plot of differentially expressed genes from the nodose ganglion and ileum mynteric iEAN. Grey dots highlight all genes analyzed by differential expression analysis. Pink dots highlight all IP-enriched genes from the ileum. Purple and blue dots highlight differentially expressed genes from nodose and ileum, respectively. Enlarged pink dots represent ileum IP-enriched transcripts expressed at higher levels than nodose. Black dots highlight neuronal genes that do not significantly differ between samples. Sample numbers are indicated in parentheses. **e**, Gene ontology pathways, identified by TopGO analysis of differentially expressed genes (log2 Fold Change > 1, padj < 0.05), enriched in the ileum (blue) vs nodose (purple). Dashed lines represent threshold of significance (1.3) as calculated by Fisher's test with an elimination algorithm. **f**, Principal Component Analysis of translatomes from the duodenum, ileum, and colon. Immunoprecipitated (IP) transcripts from myenteric iEAN (log2 Fold Change > 1, padj < 0.05) were used to generate the list of genes for comparison between all groups. **g**, Volcano plots of differentially expressed genes between the three myenteric iEAN populations. Grey dots highlight all genes analyzed by differential expression analysis. Pink dots highlight all IP-enriched genes from each pair of iEAN. Green, blue, and magenta dots represent differentially expressed genes between ileum, duodenum, and colon, respectively. Sample numbers are indicated in parentheses. **h**, Immunofluorescence staining of myenteric plexus neurons from the ileum and duodenum of C57BL/6J SPF mice using anti-somatostatin (SST) and anti-neuronal nuclear (ANNA-1) antibodies. White arrows indicate SST+ neurons. Scale bars = 50µm. Images representative of n=4 per group. **i**, Quantification of the number of SST+ neurons per mm^2 in the duodenum (n=4) and ileum (n=4) myenteric plexus of C57BL/6J SPF mice. **** $P < 0.0001$ as calculated by unpaired t-test. **j**, Immunofluorescence staining of myenteric plexus neurons from the ileum and duodenum using anti-neuropeptide Y (NPY) and anti-beta III tubulin (TUJ1) antibodies. White arrows indicate NPY+ neurons. Scale bars = 50µm. Images representative of n=2 per group.

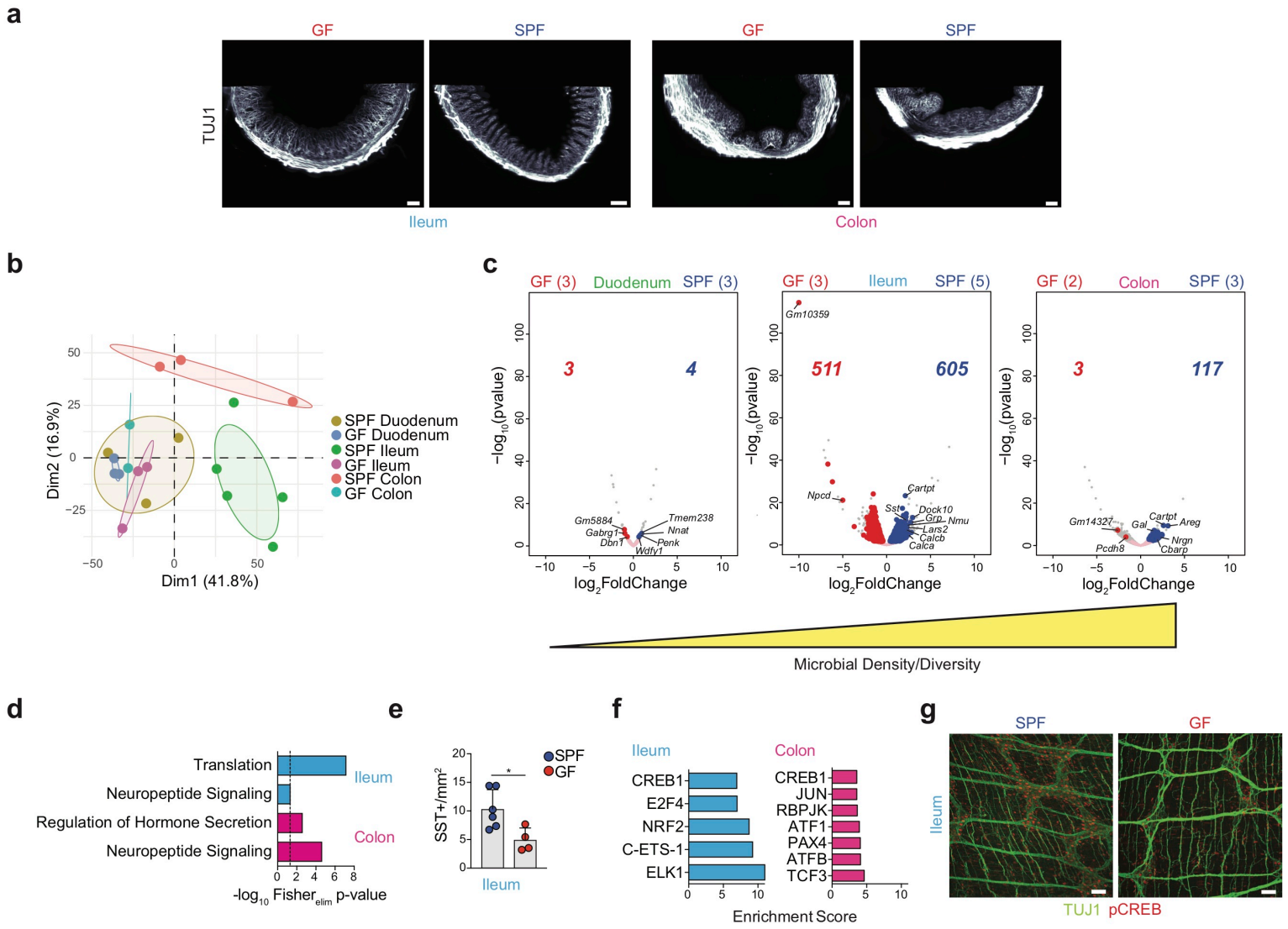

Figure 2 | Microbiota impacts iEAN translatome in a compartmentalized manner. a, AdipoClear cleared tissue Light Sheet images of the ileum and colon of C57BL/6J SPF or GF mice using anti-BIII-tubulin (TUJ1) antibody. Images representative of n=5 for all groups. Scale bar GF ileum = 200μm,SPF ileum = 200μm, GF colon = 200μm, SPF colon = 100μm. **b**, Principal Component Analysis iEAN samples from the duodenum, ileum, and colon of *Snap25*^{RiboTag} GF and SPF mice. Total comparative gene list generated from IP-enriched transcripts (log2Fold Change > 2.5, padj < 0.05) from each sample **c**. Volcano plots of differentially expressed genes of the duodenum, ileum, and colon iEAN between *Snap25*^{RiboTag} GF and SPF mice. Grey dots highlight all genes analyzed by differential expression analysis. Pink dots highlight all IP-enriched genes from the each pair of intestine segments. Red dots and number highlight genes higher in GF samples. Blue dots and number highlight genes significantly higher in SPF samples. Sample numbers are indicated in parentheses. **d**, Gene ontology pathways, identified by TopGO analysis of differentially expressed genes (log2 Fold Change > 1, padj < 0.05), enriched in SPF ileum (blue) and colon (magenta) as compared to GF samples. Dashed lines represent threshold of significance (1.3) as calculated by Fisher's test with an elimination algorithm. **e**, Numbers of SST+ neurons in the ileum myenteric plexus of GF (n=6) and SPF (n=4) mice. * $P < 0.05$ calculated by unpaired t-test. **f**, PASTAA analysis results showing enrichment of predicted CREB1 transcription factor control of the most singificantly differentially expressed genes (log2Fold Change > 1, padj < 0.05) of the ileum and colon iEAN between C57BL/6J GF and SPF mice. **g**, Immunofluorescent staining of the ileum myenteric plexus from C57BL/6J GF and SPF mice using anti-pCREB (red) and anti-TUJ1 (green) antibodies . Images representative of n=3 SPF and n=3 GF. Scale bars = 50μm.

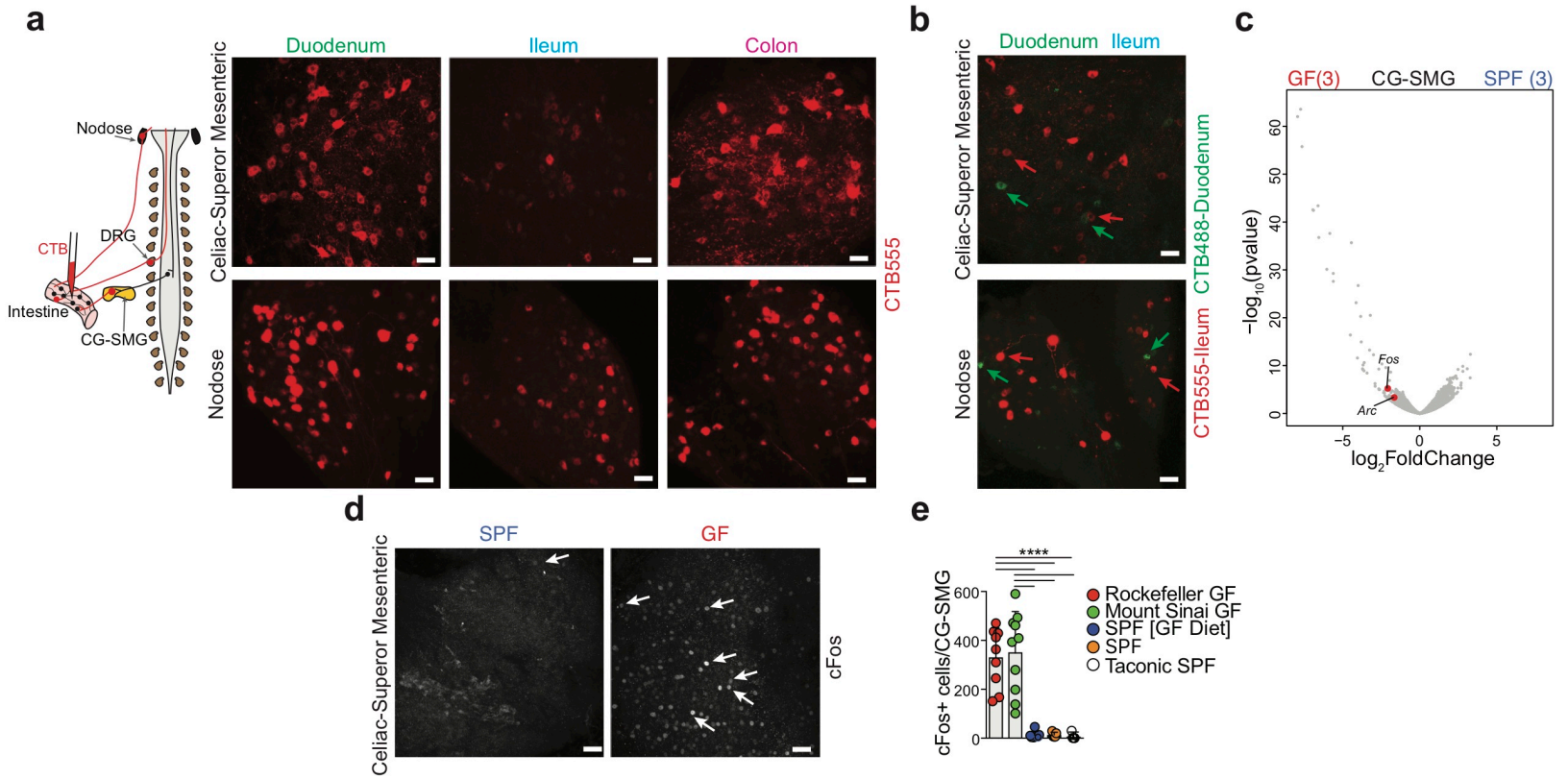

Figure 3 | Gut-associated sympathetic neurons are activated in the absence of a microbiota. a, Retrograde CTB Alexafluor555 (CTB555) tracing from the duodenum, ileum, and colon to the CG-SMG and NG of SPF mice. Scale bars = 50μm. Images representative of duodenum (n=2), ileum (n=3), and colon (n=2). **b**, Dual CTB tracing in the CG-SMG and NG with AlexaFluor488 from the duodenum and AlexaFluor555 from the ileum of SPF mice. Green arrows show duodenum-traced neurons and red arrows show ileum-traced neurons. Scale bars = 50μm. Images representative of n=2. **c**, Volcano plot of differentially expressed genes from the CG-SMG of *Snap25*^{RiboTag} GF and SPF mice. Red dots highlight the genes *Fos* and *Arc*, neuronal immediate-early genes. Sample numbers are indicated in parentheses. **d**, CG-SMG whole mount immunostaining of GF and SPF mice using anti-cFos antibody. White arrows indicate cFos+ nuclei. Scale bars = 50μm. Images representative of GF (n=9) and SPF kept on germ-free diet (n=7). **e**, Numbers of cFos+ neurons in the CG-SMG of GF mice from Rockefeller (n=9) and Mount Sinai (n=10) as compared to SPF kept on a germ-free diet (n=7), SPF normal chow (n=5), and Taconic SPF normal chow (n=5) controls. **** $P < 0.0001$ as calculated by one-way ANOVA with Tukey multiple comparisons.

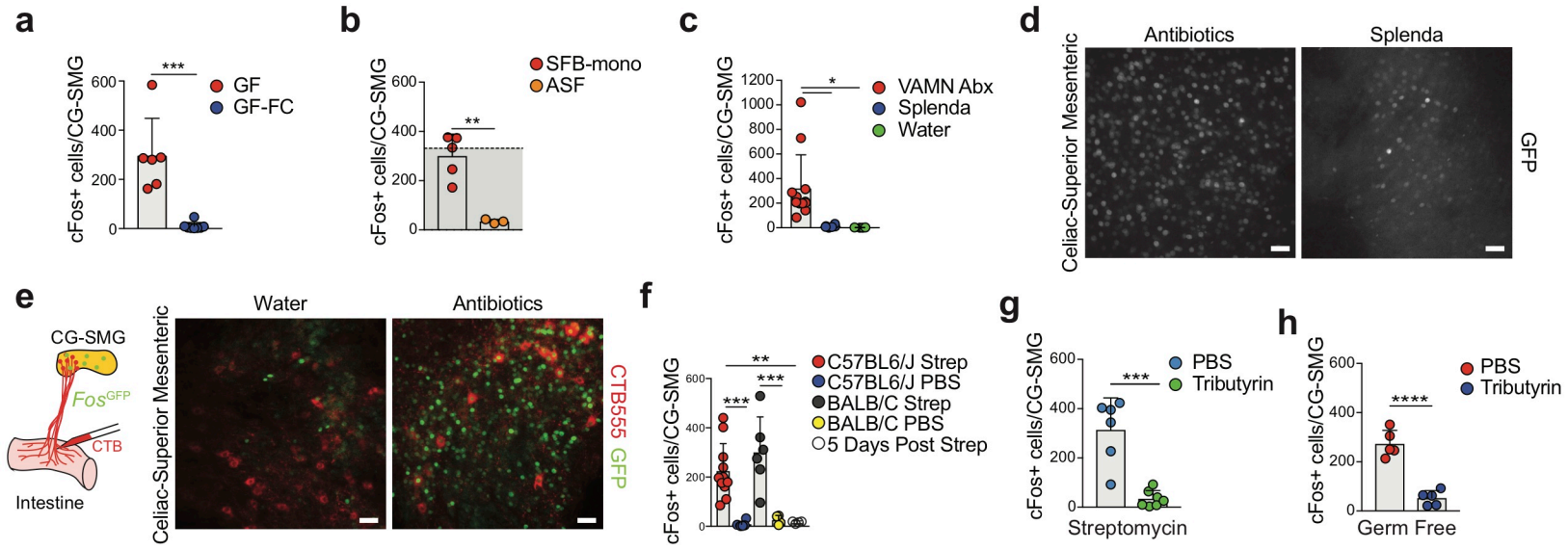

Figure 4 | Dysbiosis triggers gut sympahetic activation through loss of butyrate signal. a, cFos+ neurons in the CG-SMG of C57BL/6J GF mice (n=6) and GF mice (n=8) colonized with feces from SPF mice 2 weeks prior analysis. *** $P < 0.001$ as calculated by unpaired t-test. **b**, cFos+ neurons in the CG-SMG of C57BL/6J SFB mono-colonized mice (n=5) and ASF colonized mice (n=3). Dashed line and shaded area below indicate the average number (334) of cFos+ neurons in GF mice. ** $P < .01$ as calculated by unpaired t-test. **c**, cFos+ neurons in the CG-SMG of C57BL/6J SPF mice treated for 2 weeks with vancomycin, ampicillin, metronidazole, and neomycin (n=12) in drinking water as compared to Splenda (n=6) and water (n=5) treated controls. * $P < .05$ as calculated by one way ANOVA with Tukey's multiple comparisons. **d**, Whole mount images of CG-SMG from *Fos*^{GFP} SPF mice treated with VAMN or Splenda. Scale bars = 50μm. **e**, Whole mount of CG-SMG of *Fos*^{GFP} SPF mice treated with VAMN or water for 2 weeks, with AlexaFluor555 conjugated CTB injected into the intestine. Scale bars = 50μm. **f**, cFos+ neurons in the CG-SMG of C57BL/6J (streptomycin: n=11, PBS: n=6) or BALB/c (streptomycin: n=6, PBS: n=4) mice 24 hours post oral gavage of stremptmycin or PBS and 5 days post streptomycin in C57BL/6J mice (n=4). ** $P < .01$, *** $P < .001$ as calculated by one way ANOVA with Tukey's multiple comparisons. **g**, cFos+ neurons in CG-SMG of C57BL/6J SPF mice treated with tributyrin (n=7) or PBS (n=6) 24 hours post oral gavage of stremptmycin. *** $P < 0.001$ as calculated by unpaired t-test. **h**, cFos+ neurons in CG-SMG of C57BL/6J GF mice 24 hours post-treatment with tributyrin (n=5) or PBS (n=5). **** $P < 0.0001$ as calculated by unpaired t-test.

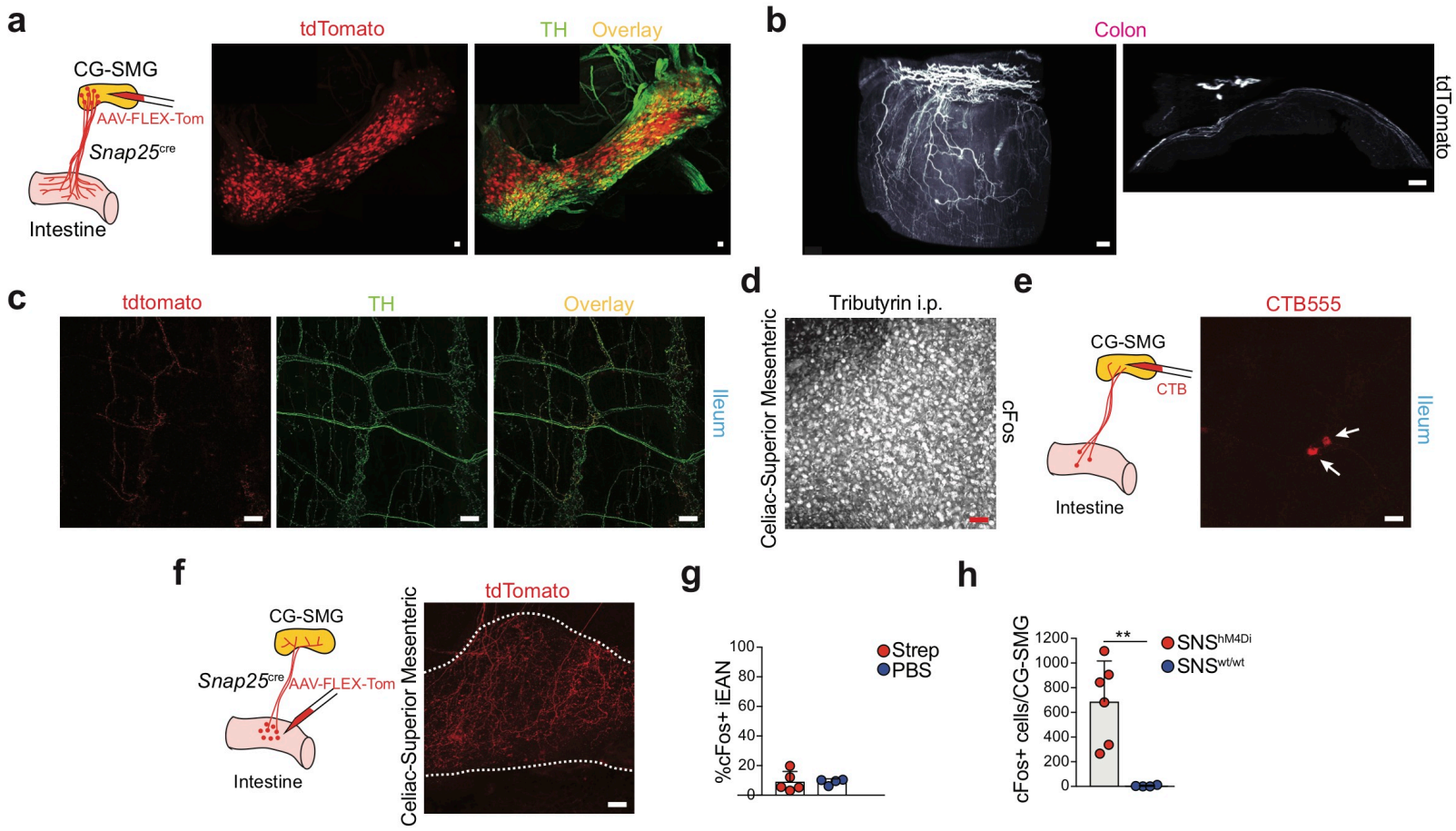

Figure 5 | Peripheral control of gut sympathetic neurons. **a**, (left) Schematic representing injection of AAVrg-CAG-FLEX-tdTomato into the CG-SMG of *Snap25*^{cre} mice to allow for tracing of fibers in the intestine. (right) Whole mount immunofluorescence of the CG-SMG with native tdTomato fluorescence (red) and staining for tyrosine hydroxylase (green). Scale bar = 50μm. Image representative of n=2. **b**, Light-sheet 3D reconstruction and optical section of the colon from **a**. Scale bar = 300μm (left image), scale bar = 200μm (right image). Image representative of n=2. **c**, Whole mount immunofluorescence of the ileum myenteric plexus from **a** with native Tomato fluorescence (red) and staining for tyrosine hydroxylase (green). Scale bar = 50μm. Image representative of n=2 **d**, Whole mount immunofluorescence of the CG-SMG staining using anti-cFos antibody after i.p. injection of tributryin. Scale bar = 50μm. Image representative of n=4. **e**, (left) Schematic representing injection of CT555 into the CG-SMG to allow for visualization of viscerofugal neurons. (right) Whole mount immunofluorescence of the ileum myenteric plexus with native CTB555 fluorescence. White arrows indicate CTB+ neurons. Scale bar = 50μm. Image representative of n=3. **f**, (left) Schematic representing injection of AAV6-CAG-FLEX-tdTomato into the intestine of *Snap25*^{cre} mice to allow for tracing of fibers. (right) Whole mount IF of CG-SMG showing tdTomato+ fibers that come, in part, from the intestine. CG-SMG is outlined with dashed lines. Scale bar = 50μm. Image representative of n=2. **g**, Percent cFos+ neurons out of ANNA-1+ neurons in the ileum myenteric plexus of C57BL/6J SPF mice 24 hours after oral gavage of streptomycin (n=5) or PBS (n=4). **j**, Numbers of cFos+ neurons in the CG-SMG of SNS^{hM4Di} (n=6) or control mice (n=4) 6 hours post Compound 21 injection. ** $P < 0.01$ as calculated by unpaired t-test.

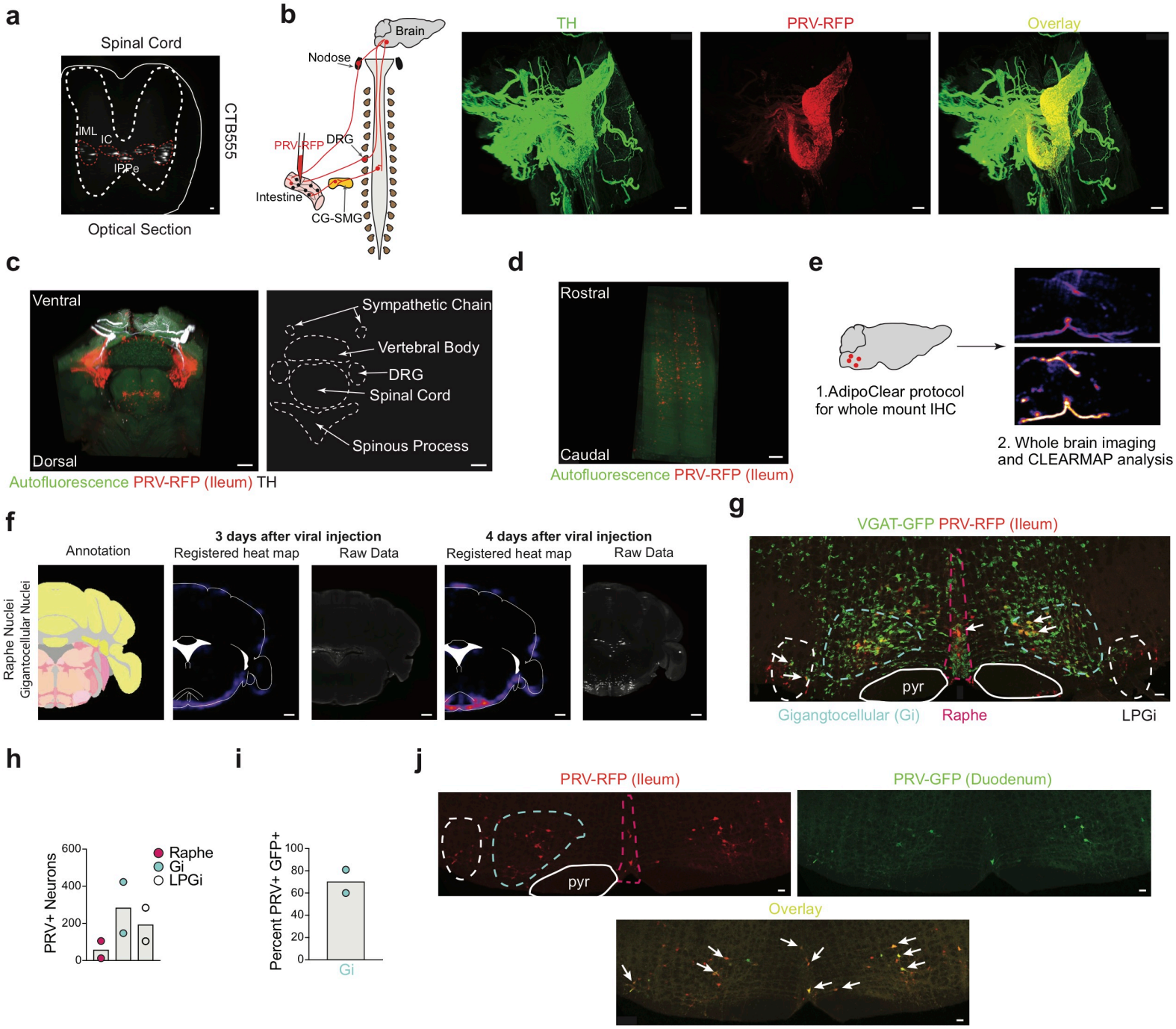

Figure 6 | CNS synaptic connections to the intestine. a, Optical section of 3DISCO cleared spinal cord showing sympathetic preganglionic neurons labeled by retrograde transport of CTB555 injected into the CG-SMG of C57BL/6J SPF mice. Scale bar = 20μm. IML=intermediolateral cell column, IC: intercalated nucleus, IPPe: central autonomic area. Image representative of n= 3. **b**, 3D reconstruction of calAdipoClear cleared CG-SMG with PRV-RFP (red) injected into the ileum 4 days post injection, stained for tyrosine hydroxylase (green). Scale bar = 300μm. Image representative of n= 3. **c**, (left) 3D reconstruction of calAdipoClear cleared intact spinal column with PRV-RFP (red) inected into the ileum 4 days post injection, stained for tyrosine hydroxylase (white). Autofluorescence in green. (right) outline of relevant spinal cord structures. Scale bars = 400μm. Image representative of n= 3. **d**, 3D cropped image of the spinal cord from **c**, showing sympathetic preganglionic neurons labeled by PRV-RFP injected into the intestine. Scale bar = 300μm. Image representative of n= 3. **e**, Schematic showing tissue clearing followed by ClearMap analysis. **f**, ClearMap analysis results of PRV-RFP injection into the ileum at days 3 and 4 post-injection showing raphe/gigantocellular nuclei. Scale bar = 1mm. Images representative of n= 3. **g**, Confocal image of native *VgatL10*^{GFP} and PRV-RFP fluorescence 4 days post-injection in a vibratome section of the brainstem. Relevant brainstem regions are highlighted. pyr = pyramidal tract, LPGi = lateral paragigantocellular nucleus. Scale bar = 50μm. Image representative of n= 2. **h**, Numbers of RFP+ cells in each of the brainstem regions highlighted in **g**. (n=2) **i**, Percentage of PRV+ *VgatL10*$^{GFP+}$ neurons in the gigantocellular nucleus, the brainstem region with the highest numbers of neurons infected. (n=2) **j**, Confocal image of native PRV-GFP (duodenum) and PRV-RFP (ileum) fluorescence 4 days post-injection in a vibratome section of the brainstem. Relevant brainstem regions are highlighted. Representative images of n=3. Scale bars = 50μm.

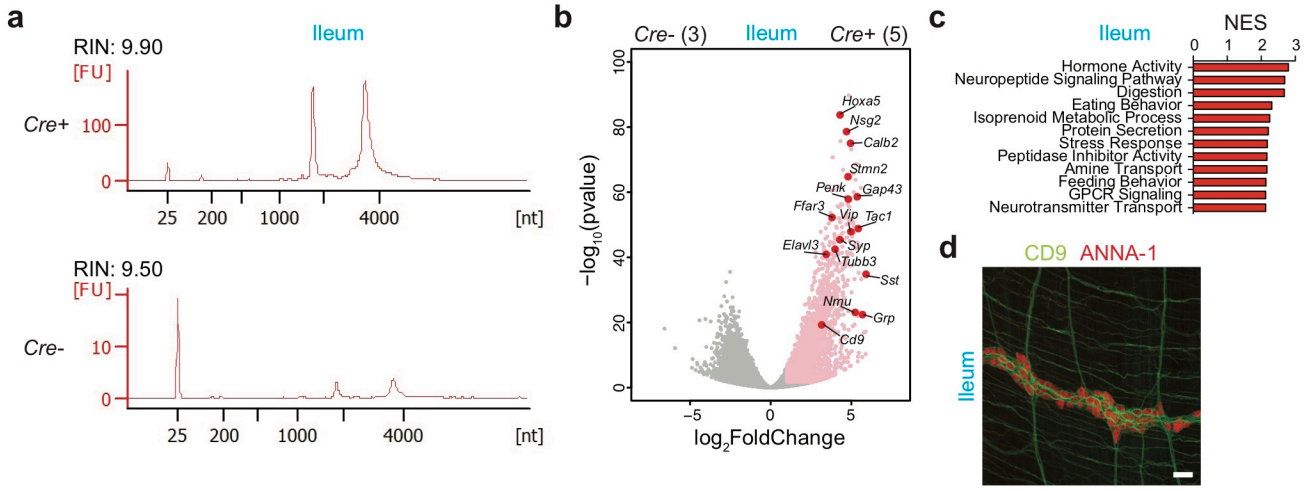

Extended Data Figure 1 | RiboTag sequencing of myenteric iEAN. a, Bioanalyzer traces of immunoprecipitated (IP) ribosome-bound mRNA eluted from the ileum *muscularis* of *Snap25*^{RiboTag} (*Cre*+) and *Snap25*^{RPL22} (*Cre*-) SPF mice. **b**, Volcano plot of differentially expressed genes between the ileum *muscularis* of *Snap25*^{RiboTag} (*Cre*+) and *Snap25*^{RPL22} (*Cre*-) mice. Pink dots highlight those transcripts with a log2 Fold Change of >1 and a p-value of <0.05. Red dots and black labels highlight select IP enriched genes. Number of samples shown in parentheses. **c**, Graph of the top 12 gene ontology pathways with a FDR < 25% identified by Gene Set Enrichment Analysis (GSEA) from ileum IP-enriched genes (log2 Fold Change > 1, padj < 0.05). NES, normalized enrichment score; FDR, false detection rate. **d**, Whole mount immunofluorescence of the ileum myenteric plexus of C57BL/6J SPF mice using anti-CD9 (in green) and anti-neuronal-specific ANNA-1 (in red). Scale bar, 50 μm. Image representative of duodenum and colon mytenteric plexus and n = 2.

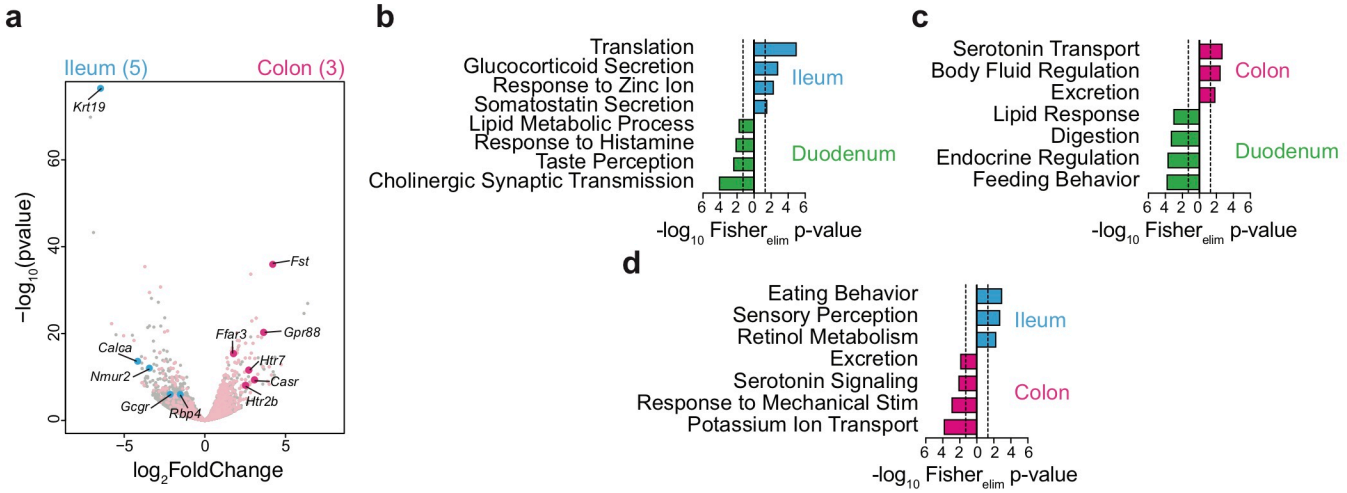

Extended Data Figure 2 | iEAN anatomical differences in gene expression and pathways. a, Volcano plot of differentially expressed genes between the ileum and colon iEAN of *Snap25*^{RiboTag} SPF mice. Grey dots highlight all genes analyzed by differential expression analysis. Pink dots highlight all IP-enriched genes from the ileum and colon. Magenta and blue dots highlight differentially expressed genes between colon and ileum, respectively. Sample numbers are indicated in parentheses. **b**, Gene ontology pathways, identified by TopGO analysis of differentially expressed genes (log2 Fold Change > 1, padj < 0.05), enriched in the ileum (blue) vs duodenum (green). Dashed lines represent threshold of significance (1.3) as calculated by Fisher's test with an elimination algorithm. **c**, Gene ontology pathways, identified by TopGO analysis of differentially expressed genes (log2 Fold Change > 1, padj < 0.05), enriched in the colon (magenta) vs duodenum (green). Dashed lines represent threshold of significance (1.3) as calculated by Fisher's test with an elimination algorithm. **d**, Gene ontology pathways, identified by TopGO analysis of differentially expressed genes (log2 Fold Change > 1, padj < 0.05), enriched in the ileum (blue) vs colon (magneta). Dashed lines represent threshold of significance (1.3) as calculated by Fisher's test with an elimination algorithm.

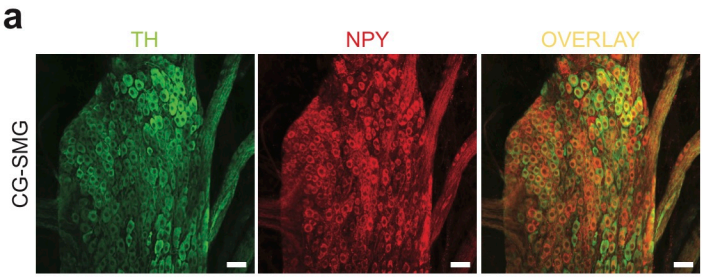

Extended Data Figure 3 | NPY is also a marker for CG-SMG neurons. a, Whole mount immunofluorescence of the CG-SMG from C57BL/6J SPF mice using anti-tyrosine hydroxylase (TH, in green) and anti-neuropeptide Y (NPY, in red) antibodies. Scale bar, 50 μm. Image representative of n=2.

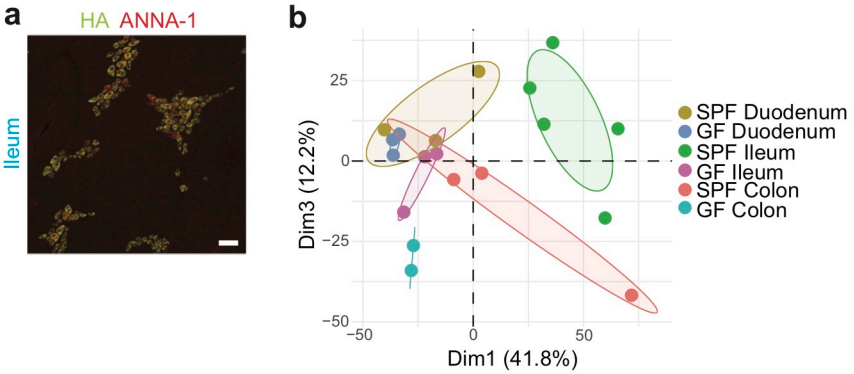

Extended Data Figure 4 | Rederivation of *Snap25*^{RiboTag} mice into Germ-Free Conditions. a, Expression of HA in ileum myenteric neurons of *Snap25*^{RiboTag} GF mice. Scale bar = 50μm. Image representative of duodenum and colon mytenteric plexus and n = 2. **b**, Principal Component Analysis, with components 1 and 3, of GF and SPF iEAN from the duodenum, ileum, and colon. Total comparative gene list generated from IP enriched transcripts (log2Fold Change > 2.5, padj < 0.05) from each sample.

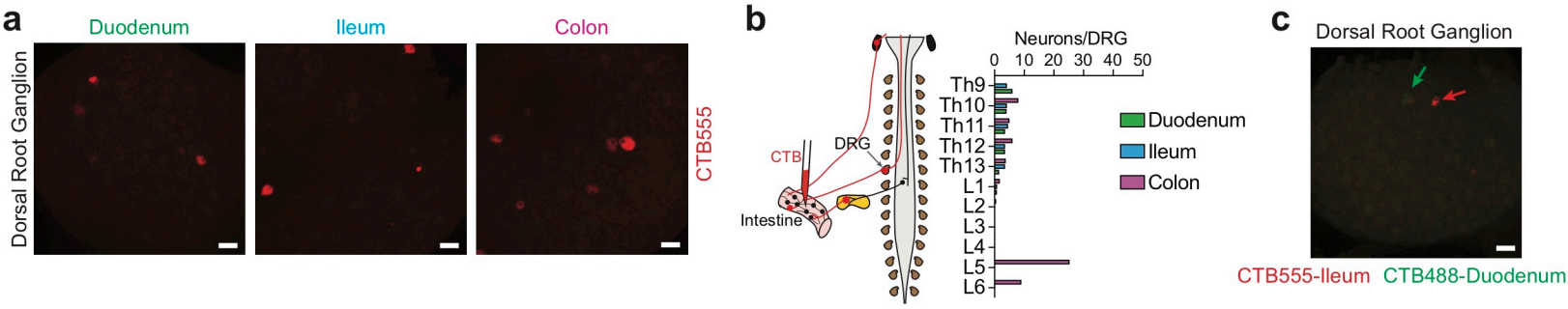

Extended Data Figure 5 | Distribution and organization of DRG innervating the intestine. a, Retrograde CTB Alexafluor555 (CTB555) tracing from the duodenum, ileum, and colon to the thoracic 10 DRG of C57BL/6J SPF mice. Scale bars = 50μm. Images representative of duodenum (n=2), ileum (n=3), and colon (n=2). **b**, Distribution of CTB555 retrograde traced neurons in the DRG from injections in the duodenum (n=2), ileum (n=3), and colon (n=2). **c**, Dual CTB tracing in the thoracic 9 DRG with AlexaFluor488 from the duodenum and AlexaFluor555 from the ileum. Green arrows show duodenum traced neurons and red arrows show ileum traced neurons. Scale bar = 50μm. Image representative of n=2.

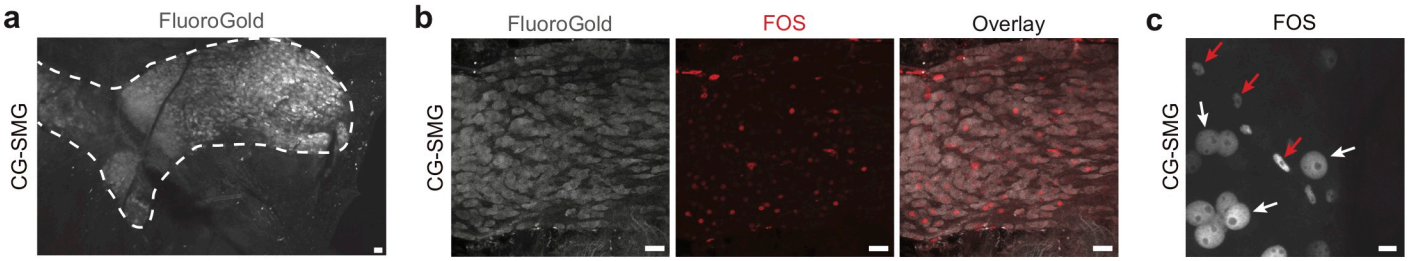

Extended Data Figure 6| Identification of CG-SMG neuronal cFos+ nuclei. a, Native fluorescence of FluoroGold in a whole mount preparation of the CG-SMG from C57BL/6J SPF mice 3 days after after i.p. injection. Dotted line outlines the CG-SMG FluoroGold+ signal. Scale bar = 50μm. Image representative of n=4. **b**, Whole mount immunofluorescence of CG-SMG from an acutely stressed C57BL/6J SPF mouse. Stained for cFos (red) and native fluorescence of FluoroGold. Scale bars = 50μm. Image representative of at least n=4. **c**, Whole mount immunofluorescence of CG-SMG from an acutely stressed mouse. Stained for cFos (white). White arrows indicate neuronal cFos+ nuclei, red arrows indicate non-neuronal cFos+ nuclei. Scale bar = 10μm.

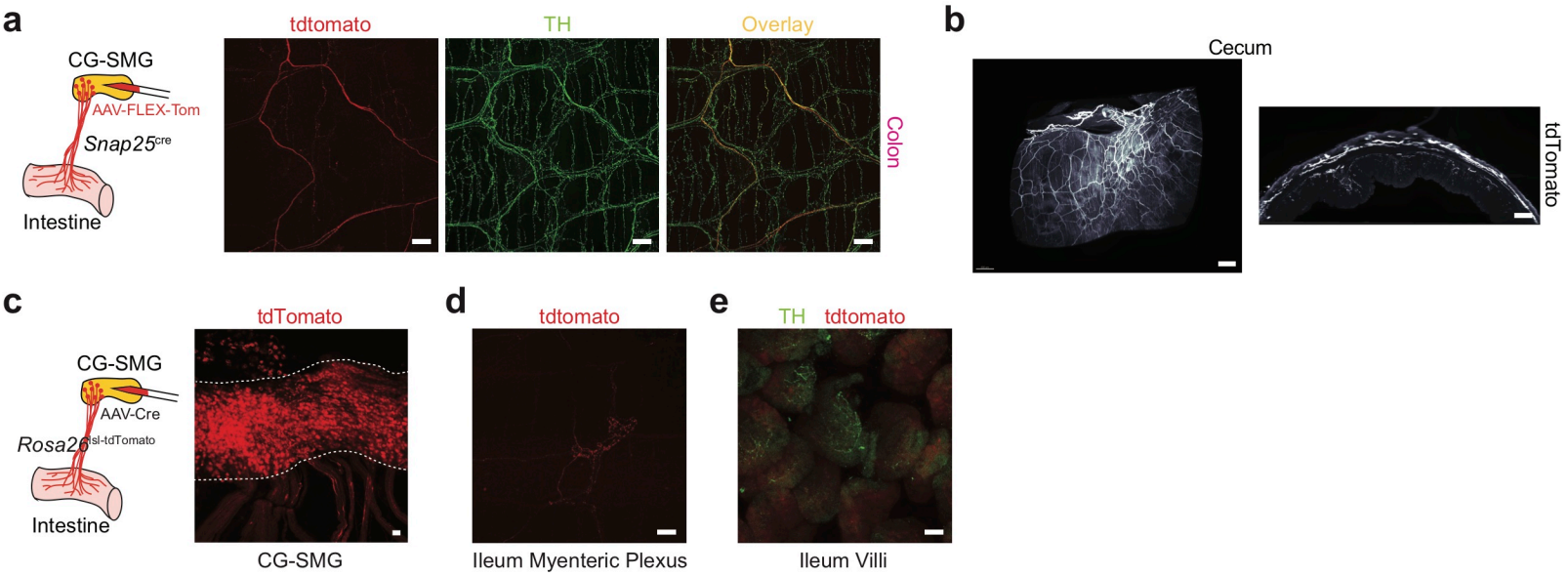

Extended Data Figure 7 | Tracing of CG-SMG fibers in the intestine. **a**, (left) Schematic representing injection of AAVrg-CAG-FLEX-tdTomato into the CG-SMG of *Snap25*^{cre} mice to allow for tracing of fibers in the intestine. (right) Whole mount immunofluorescence of the colon myenteric plexus with native Tomato fluorescence (red) and staining using anti-tyrosine hydroxylase (green) antibody. Scale bar = 50μm. Image representative of n=2. **b**, Light-sheet 3D reconstruction and optical section of the cecum from **a**. Scale bar = 500μm (left image), scale bar = 200μm (right image). Image representative of n=2. **c**, (left) Schematic representing injection of AAVrg-hSyn1-Cre in to the CG-SMG of *Rosa26*$^{lsl\text{-}tdTomato}$ mice to allow for tracing of fibers in the intestine. (right) Whole mount of the CG-SMG with native Tomato fluorescence (red). Scale bar = 50μm. Image representative of n=2. **d**, Whole mount immunofluorescence of the ileum myenteric plexus with native Tomato fluorescence (red) from **c**. Scale bar = 50μm. Image representative of n=2. **e**, Whole mount immunofluorescence of the ileum villi with native Tomato fluorescence (red) and staining using anti-tyrosine hydroxylase (green) antibody, from **c**. Scale bar = 50μm. Image representative of n=2.

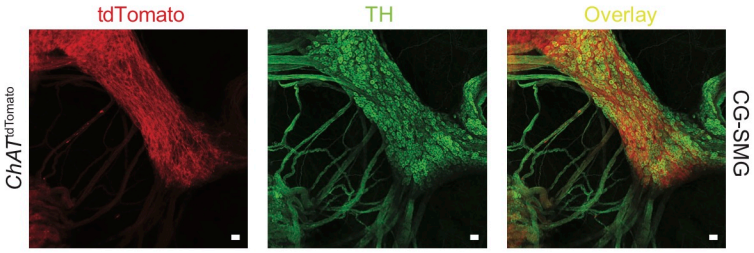

Extended Data Figure 8 | Cholinergic input to the CG-SMG. **a**, Whole mount immunofluorescence of the CG-SMG from *Chat*^{tdTomato} mice with native Tomato fluorescence (red) and staining with anti-tyrosine hydroxylase (green) antibody. Scale bar = 50μm. Image representative of n=2.

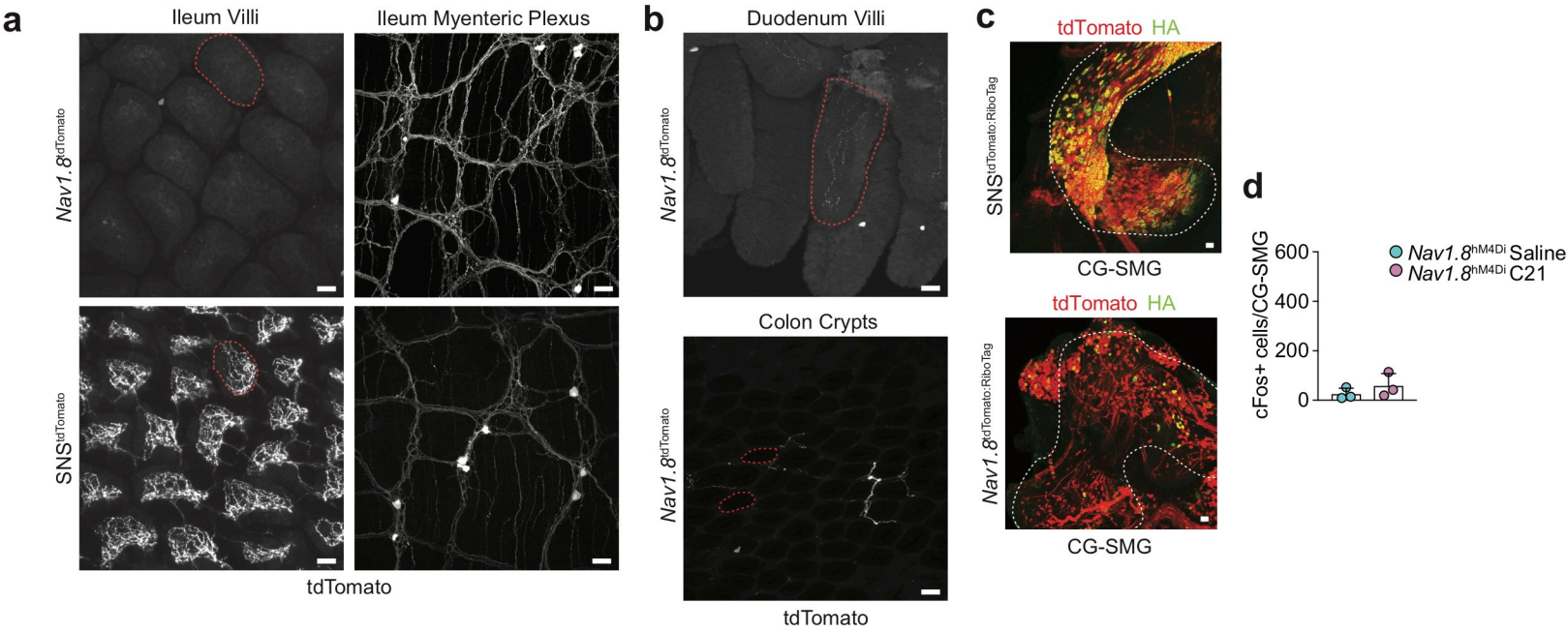

Extended Data Figure 9 | Specificity of sensory neuron Cre drivers. a, Whole mount images of native tdTomato fluorescence in ileum villi and myenteric plexus from *Nav1.8*^{tdTomato} and SNS^{tdTomato} mice. Red dashed lines highlight villi structure. Scale bars = 50μm. Images representative of n=3. **b**, Whole mount images of native tdTomato fluorescence in duodenum villi and colon crypts from *Nav1.8*^{tdTomato} mice. Red dashed lines highlight villi structure in the duodenum and crypt in the colon. Scale bars = 50μm. Images representative of n=3. **c**, Whole mount immunofluorescence with native Tomato fluorescence (red) and staining with anti-HA (green) antibody in the CG-SMG of *Nav1.8*$^{tdTomato:RiboTag}$ and SNS$^{tdTomato:RiboTag}$ mice. White dashed lines outline the CG-SMG. Scale bars = 50μm. Images representative of n=2. **d**, Numbers of cFos+ neurons in the CG-SMG of *Nav1.8*^{hM4Di} 6 hours post Compound 21 or saline injection. n=3 per group.

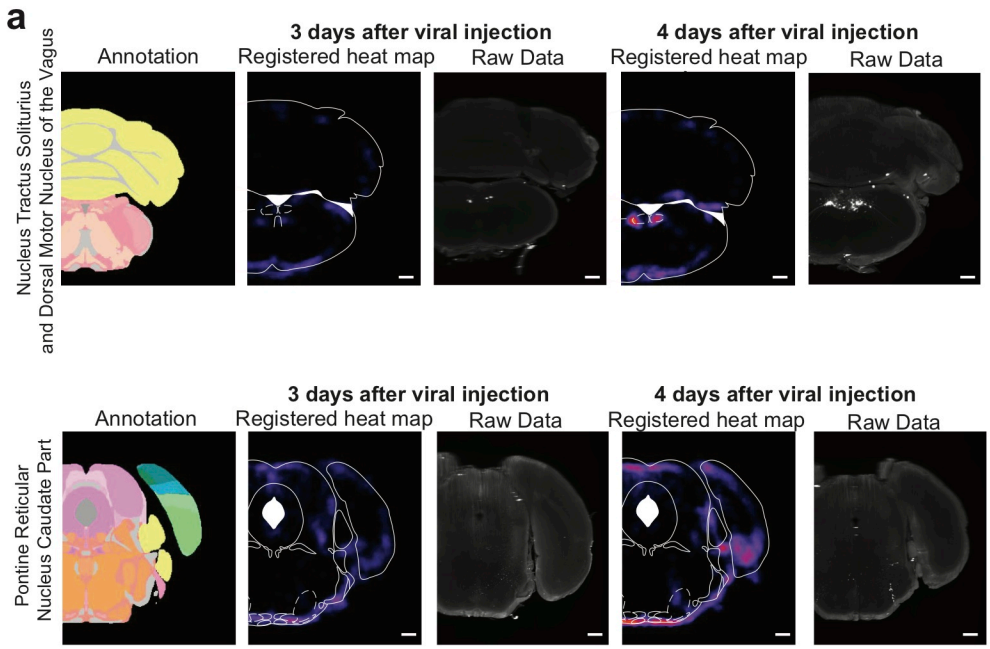

Extended Data Figure 10 | ClearMap analysis of ileum PRV-RFP injection. a, ClearMap analysis results of PRV-RFP injection into the ileum of C57BL/6J SPF mice at days 3 and 4 post-injection showing nucleus tractus solitarius/dorsal motor nucleus of the vagus nerve (top) and the caudal pontine reticular nucleus (bottom). Scale bars = 1mm. Images representative of n= 3.

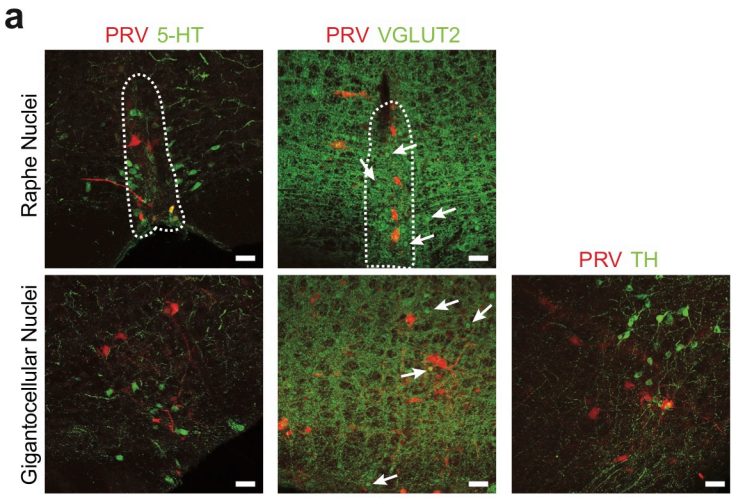

Extended Data Figure 11 | a, Immunofluorescent images for neuronal subsets within the raphe and gigantocellular nuclei in mice with PRV-RFP injected in the ileum of C57BL/6J SPF mice. Native fluorescence for RFP (red) and stained with anti-5-HT (green), anti-Vglut2 (green), and anti-TH (green) antibodies. Dashed lines highlight raphe nuclei. White arrows indicate VGLUT2+ cells. Scale bars = 50μm. Images representative of n=2-3.

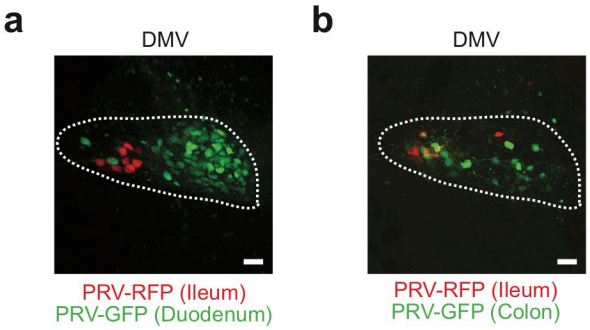

Extended Data Figure 12 | Separate parasympathetic input to the intestine. a, Confocal image of the caudal brainstem. Dual PRV injection into the ileum (PRV-RFP) and duodenum (PRV-GFP) of C57BL/6J SPFat 4 days leads to infection of separate populations of neurons in the dorsal motor nucleus of the vagus nerve (DMV). Dashed line outlines the borders of the DMV. Scale bar = 50μm. Image representative of n=3. **b**, Confocal image of the caudal brainstem. Dual PRV injection into the ileum (PRV-RFP) and colon (PRV-GFP) at 4 days leads to infection of separate populations of neurons in the dorsal motor nucleus of the vagus nerve (DMV). Dashed line outlines the borders of the DMV. Scale bar = 50μm. Image representative of n=3.